

Roto-Translation Equivariant Super-Resolution of Two-Dimensional Flows Using Convolutional Neural Networks

Yuki Yasuda^{a)}

(*Electronic mail: yasuda.y.aa@m.titech.ac.jp)

(Dated: 10 March 2022)

Convolutional neural networks (CNNs) often apparently process vectors as quantities that have no direction such as colors in images. This study investigates the effect of considering vectors as geometric objects in terms of super-resolution of velocity on two-dimensional fluids. Vector is distinguished from scalar by the transformation law associated with a change in basis, which can be incorporated as the prior knowledge using the equivariant deep learning. The existing CNNs are converted into equivariant ones by rendering each layer equivariant with respect to rotation and translation. The training data in the low- and high-resolution are generated with the downsampling or spectral nudging. With the date inheriting the rotational symmetry, the equivariant CNNs exhibit comparable accuracy with the non-equivariant ones. Owing to the smaller number of parameters in the equivariant CNNs, these models are trainable with a smaller size of the data. In this case, the transformation law of vector should be incorporated as the prior knowledge, where vector is treated as a quantity having direction. Two examples are presented to demonstrate the possibility of symmetry of the data being broken. In the first case, the downsampling method renders the correspondence between low- and high-resolution patterns dependent on the orientation. In the second case, the input data are insufficient to recognize the rotation of coordinates. In both cases, the accuracy of the CNNs deteriorates if the equivariance is forcefully imposed, and the conventional CNNs should be used, where vector is not processed as a quantity having direction.

I. INTRODUCTION

In recent years, neural networks (NNs) have been actively applied to the field of fluid mechanics.^{1–4} The physical validity of inference of NNs is important both in theory and application. One method to enhance the validity involves explicitly incorporating physics laws such as the Navier-Stokes equations into NNs, which is referred to as the physics-informed neural network⁵. This method has been extensively studied recently.^{6,7}

Vector is an essential quantity in physics. However, in applications of NNs to fluids, vectors are often apparently processed as direct products of scalars such as colors in images, and convolutional neural networks (CNNs) are employed as in computer vision. Intuitively, vector has direction, whereas scalar does not. This distinction can be mathematically formulated by covariance in geometry.^{8,9} The covariance describes the manner in which the components of a tensor (e.g., scalar and vector) change under a change of basis associated with a certain coordinate transformation. These transformation laws distinguish the rank of tensors and can be regarded as a part of the definition of scalars and vectors.¹⁰ In other words, by changing the direction of observation through a coordinate transformation, it is possible to determine whether a numerical array is a combination of scalars or a vector having a direction.

The covariance ensures that scalar and vector themselves are geometrically invariant objects, although their components may be changed under coordinate transformations. Consequently, this leads to the invariance of physics laws de-

scribed with scalars and vectors; that is, the forms of physics equations are independent of coordinate systems. On incorporation of both covariance and physics laws into NNs as prior knowledge, the NNs can be applied to data on any coordinate system without compromising on the accuracy and physical validity. Such NNs incorporating geometric symmetries have been applied to various systems^{11,12} including fluid systems.^{13–18}

Super-resolution (SR) refers to methods of estimating high-resolution images from those with low-resolution. Super-resolution is studied in computer vision as an application of NNs.^{19–23} The success of such NNs has resulted in an increased number of studies that have focused on the fluid-related SR: idealized turbulent flows in two^{24–30} and three dimensions,^{28,29,31–33} Rayleigh–Bénard convection,³⁴ smoke motions in turbulent flows,^{35–37} flows in blood vessels,^{38–40} sea surface temperature,^{26,41} and atmospheric fields.^{42–49} Physics laws such as the continuity equation can be considered as the prior knowledge, rendering super-resolved flows more accurate and physically valid.^{27,32,40} However, studies related to investigating SR models in terms of geometry are scarce, and the invariance of physics equations has yet to be fully exploited.

The covariance in super-resolution can be satisfied by imposing the equivariance on NNs. For instance, if an NN is equivariant, rotating the input results in the output being rotated in the same manner (Fig. 1). Therefore, if the input is a vector field, the output satisfies the same transformation law, assuring that the output is a geometric vector field.

The success of conventional CNNs can be attributed to the translation equivariance. CNNs with other types of equivariance (e.g., rotation) have also been studied.^{50–57} These CNNs can be understood within unified frameworks on the equivariant CNN^{58–60} that are based on the group theory^{61,62} and differential geometry.^{8,9} The theories and techniques on the

^{a)}Global Scientific Information and Computing Center, Tokyo Institute of Technology, 2-12-1 Ookayama, Meguro-ku, Tokyo 1528550, Japan

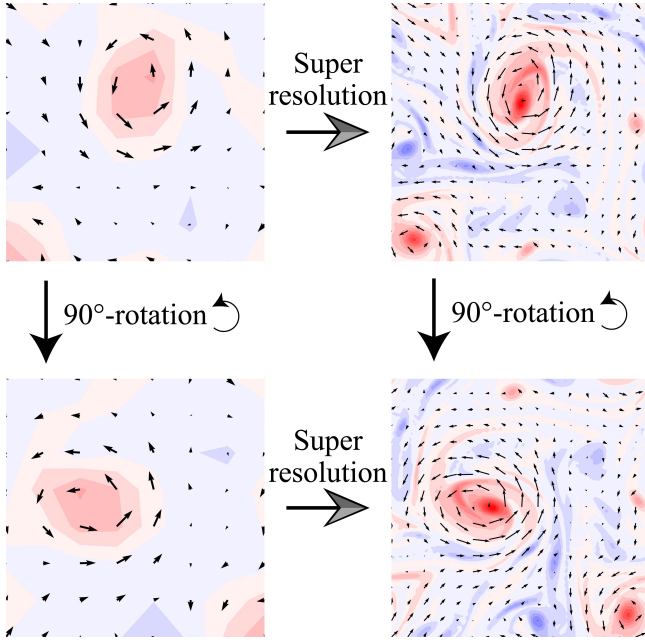


FIG. 1. Schematic for the equivariance of super-resolution. If a super-resolution model is equivariant, the rotation is commutative with the super-resolution. The anti-clockwise rotation by 90° is considered here. The colors represent a scalar field and the arrows represent a vector field.

equivariant CNN have been developed for two-dimensional images, three-dimensional volumetric data⁶³ and point cloud data⁶⁴, and graph data.⁶⁵ These studies are considered as a part of the geometric deep learning.^{11,12}

Herein, studies related to equivariant NNs are briefly reviewed from an application perspective. These studies can be categorized into two: studies on super-resolution in computer vision and studies employing equivariant NNs in fluid mechanics. The latter does not include the fluid SR.

Certain studies have used the concept of equivariance on super-resolution, including image-reconstruction, in computer vision. Xie et al.⁶⁶ proposed a new self-attention module and reconstructed high-resolution images. In their module, the point-wise convolution was utilized to construct key, query, and value, resulting in the equivariance to any pixel permutation. Lee and Lee⁶⁷ developed a new discriminator based on the rotation invariance and hierarchy of scale. The generative adversarial networks (GANs) reproduced more realistic images by replacing only the discriminator with their new one. Chen et al.⁶⁸ incorporated the equivariance loss to reduce the degrees of freedom of the inverse problem and demonstrated that the image reconstruction was possible with unsupervised learning. In a subsequent study,⁶⁹ they enhanced the robustness of inference via the introduction of an estimator into the loss, which reflected the reconstruction error. Remedios et al.⁷⁰ proposed the crop-equivariance and implemented a crop-equivariant CNN using valid convolutions. A concatenated image after the super-resolution was the same as the super-resolved image of the full size without cropping. The above studies^{66–70} did not employ the equivariant CNN^{58–60} in the

image generation and did not super-resolve vector fields; from these perspectives, the present study is distinguished.

In fluid mechanics, several studies employed equivariant NNs. Ling et al.⁷¹ estimated the Reynolds stress tensor of three-dimensional turbulence using a multilayer perceptron. Their model inferred the coefficients of the Reynolds stress described with the tensor bases. The theory guarantees the rotation equivariance and Galilean invariance via changes in the basis tensors. Gao et al.¹³ developed the theory and algorithm on a rotation equivariant NN. They confirmed the error reduction and rotation equivariance by conducting various case studies; e.g., the inference of the strain tensor from the electrostriction fourth-order tensor. Wang et al.¹⁴ incorporated various symmetries into CNNs and demonstrated that the generalizability and accuracy of future predictions were improved for two-dimensional convection and ocean current. Suk et al.¹⁵ proposed a surrogate model using equivariant and anisotropic graph convolutions. They successfully predicted a vector quantity: wall shear stress, on the surface of three-dimensional arteries. Siddai et al.¹⁶ developed an equivariant CNN and estimated three-dimensional steady flows around several particles from the particle positions, mean flow, and Reynolds number. Han et al.¹⁷ improved the vector-cloud network to be equivariant to rotation. Their model emulated the three-dimensional Reynolds stress with high accuracy. Pawar et al.¹⁸ proposed a subgrid-scale model for the two-dimensional turbulence using an equivariant CNN. Their model was accurate and yielded stable energy spectra for the various Reynolds numbers. The above studies^{13–18,71} suggest that the incorporation of physics symmetries enhances the accuracy and robustness of inference. However, to the best of the authors' knowledge, the effect of including symmetries has not been sufficiently examined in terms of the fluid SR.

This study investigated the equivariance on the super-resolution of two-dimensional fluids by employing two existing CNNs by Fukami et al.²⁵ and Bode et al.³² The equivariance to rotation and translation was considered by utilizing the theory and software library developed by Weiler and Cesa.⁶⁰ Two types of low- and high-resolution data were used. For the first type, only the high-resolution (HR) flow was generated from the fluid simulation, and the low-resolution (LR) flow was obtained by downsampling. In contrast, for the other type, first, the LR flow was generated from the fluid simulation, and subsequently, the HR flow was obtained from another simulation including a spectral nudging.^{72,73} The results presented here can be referred to when an SR model is built for climate data because large-scale flows in the ocean and atmosphere can be approximately regarded as two-dimensional (i.e., geostrophic flows).

This study demonstrates the following three things:

- The equivariance of super-resolution depends on the following: the intrinsic symmetry of fluid systems, the generation method of LR and HR data, and the choice of input data.
- When the super-resolution is equivariant, the accuracy of the equivariant CNNs is comparable to that of the non-equivariant ones. Further, the equivariant CNNs

are trainable with a smaller size of the data owing to the reduction in the learnable parameters.

- In case the super-resolution is not equivariant, the accuracy of the equivariant CNNs is lower than that of the non-equivariant ones. Conventional CNNs should be used, where vector is treated as a quantity having no direction.

The remaining paper is organized as follows. Section II clarifies the covariance and equivariance and describes the procedure for rendering the existing CNNs^{25,32} equivariant. Section III presents the methods for training and evaluating the CNNs. Section IV compares the equivariant and non-equivariant CNNs when the data have the rotational symmetry. Section V discusses two examples where the data do not have the rotational symmetry and the super-resolution is not equivariant. The conclusions are presented in Section VI. The source code is available on the GitHub repository.⁷⁴

II. ROTO-TRANSLATION EQUIVARIANT CNNS

The mathematical notations and terms used in this study are clarified followed by a discussion on equivariant CNNs. The covariance and equivariance are defined in Section II A. The non-equivariant and equivariant CNNs are presented in Section II B.

This study considers the two-dimensional Euclidean space using the Cartesian coordinate system: $\mathbf{x} = (x, y)^T \in \mathbb{R}^2$. A combination of translation and rotation is represented by the special Euclidean group $SE(2)$ or a subgroup of $SE(2)$. Scalar (i.e., tensor of rank 0) and vector (i.e., tensor of rank 1) are considered; however, higher-rank tensors are excluded here. Contravariant and covariant vectors are identified because of the orthonormal basis on the Cartesian coordinates. There are two types of transformations in the tensor analysis: active and passive transformations. In the former, scalar and vector themselves are transformed, whereas the coordinates remain fixed. In contrast, in case of the latter, the opposite treatment is adopted. The active transformation is employed following the previous studies on the equivariant CNNs.^{59,60} When using the passive transform, it is stated clearly.

A. Covariance and equivariance

Covariance and equivariance are clarified for this study. Mathematical detail can be further clarified referring to Refs. 8, 9, 11, and 60.

The translation and rotation are defined using a position vector $\mathbf{x} = (x, y)^T$:

$$\tau_t \mathbf{x} = \mathbf{x} + \mathbf{t}, \quad (1a)$$

$$\rho_\theta \mathbf{x} = \begin{pmatrix} \cos(\theta) & -\sin(\theta) \\ \sin(\theta) & \cos(\theta) \end{pmatrix} \begin{pmatrix} x \\ y \end{pmatrix}, \quad (1b)$$

where \mathbf{t} is a translation vector and θ is a rotation angle. The inverse transforms are represented as $\tau_t^{-1} \mathbf{x} = \tau_{-\mathbf{t}} \mathbf{x}$ and

$\rho_\theta^{-1} \mathbf{x} = \rho_{-\theta} \mathbf{x}$. A combination of translation and rotation is formulated as follows:

$$\tau_t \rho_\theta \mathbf{x} = (\rho_\theta \mathbf{x}) + \mathbf{t}. \quad (2)$$

If there is no confusion, the subscripts of \mathbf{t} and θ are omitted.

The covariance provides the transformation laws for a scalar $\omega(\mathbf{x})$ and a vector field $\mathbf{v}(\mathbf{x})$ under rotation and translation:

$$g_{\text{scalar}}: \omega(\mathbf{x}) \mapsto \omega((\tau \rho)^{-1} \mathbf{x}) [= \omega(\rho^{-1}(\mathbf{x} - \mathbf{t}))], \quad (3a)$$

$$g_{\text{vector}}: \mathbf{v}(\mathbf{x}) \mapsto \rho \mathbf{v}((\tau \rho)^{-1} \mathbf{x}) [= \rho \mathbf{v}(\rho^{-1}(\mathbf{x} - \mathbf{t}))], \quad (3b)$$

$$g: F(\mathbf{x}) \mapsto \pi(\rho) F((\tau \rho)^{-1} \mathbf{x}) [= \pi(\rho) F(\rho^{-1}(\mathbf{x} - \mathbf{t}))] \quad (3c)$$

Only the referred position is changed for a scalar as in (3a), whereas in case of a vector, both the referred position and components are changed as in (3b). The change in the vector components describes the change in its direction. When scalars or vectors are piled onto a numerical array, each is independently transformed according to (3a) and (3b). Both scalars and vectors satisfy the linearity. The transformation law, that is, covariance, distinguishes between scalar and vector. The last equation (3c) can be used to any combination of any tensor fields, where the representation of $\pi(\rho)$ depends on F : $\pi(\rho) = 1$ for a scalar; $\pi(\rho) = \rho$ for a vector; $\pi(\rho)$ is a block diagonal matrix consisting of ρ when F is a stack of vectors.

The equivariance is defined as the commutativity of a function f with transformations g . Consider a function $f: X_{\text{in}} \mapsto X_{\text{out}}$, where X_{in} is a scalar or vector field and for simplicity X_{out} is assumed to be a field of the same type as X_{in} . The function f is equivariant if it satisfies

$$(f \circ g)(X_{\text{in}}) = (g \circ f)(X_{\text{in}}) = g(X_{\text{out}}), \quad (4)$$

where the representation of g is determined by X_{in} and X_{out} . Equation (4) implies that f is equivariant if f is commutative with g . The transformation g composes a group such as $SE(2)$, and Eq. (4) must hold for all elements of the group. When g represents a rotation, for instance, the rotated input $g(X_{\text{in}})$ yields the output $f(g(X_{\text{in}}))$, which is equal to the rotated output $g(f(X_{\text{in}}))$ (Fig. 1). Note that invariance is a special case of the equivariance: $(f \circ g)(X_{\text{in}}) = X_{\text{out}}$, where the output is a constant field. The entire neural network is equivariant if each layer satisfies the equivariance.^{11,60}

B. Method of constructing equivariant CNNs

The equivariant CNNs used in this study were obtained from existing CNNs by rendering each layer equivariant. Many network architectures for the super-resolution have been proposed. To fully exploit those results, the influence of converting the proposed networks to equivariant ones must be examined. Two CNNs were employed: hybrid downsampled skip-connection/multi-scale (DSC/MS) model by Fukami et al.²⁵ and residual in residual dense network (RRDN) by Bode et al.³² The details on the network architectures are presented

in Appendix A. The input of both models is a snapshot of either velocity or vorticity and the output is the super-resolved field at the instantaneous time.

The hybrid DSC/MS model (hereafter, DSC/MS) was proposed in pioneering work on the fluid SR by Fukami et al.²⁵ They combined their model of downsampled skip connection (DSC) with the multi-scale (MS) model.⁷⁵ Multi-scale signals in a fluid field can be captured by the downsampling and skip connections in the DSC/MS. They reported that the DSC/MS super-resolved both velocity and vorticity fields in two dimensions. In the subsequent studies, the DSC/MS was applied to the three-dimensional velocity^{28,29}; the spatio-temporal SR was performed by the successive use of DSC/MS in space and time;²⁹ a deeper version of DSC/MS was proposed.³⁰ Although the DSC/MS has been proposed relatively early, it is still among the most important CNNs in the field of fluid SR.

The RRDN utilizes residual in residual dense block (RRDB),^{21,76} which extracts multi-scale structures in a fluid field with dense skip connections. Bode et al.³² proposed the RRDN as the generator of their physics-informed GAN and applied their GAN to the three-dimensional velocity. A similar network to the RRDN was employed for the SR of two-dimensional passive scalars.²⁷ The RRDB, which is the core module of the RRDN, has been utilized for the SR in fluid mechanics^{27,32} as well as in computer vision.^{21,76} Thus, an equivariant CNN having RRDBs needs to be investigated.

The discretization of rotation and the group representation are discussed before explaining the procedure to create the DSC/MS and RRDN equivariant. In practice, scalar and vector fields need to be discretized in space, and the rotation acting on them is discretized as well. This study focuses on the discrete rotation in multiples of 90° or 180°. These rotations do not require interpolation or extrapolation and are easily made commutative with downsampling such as the local average (Section V A). The rotations in multiples of 90° and 180° are mathematically described by the cyclic groups of order 4 and 2 (i.e., C_4 and C_2), respectively. Further, CNNs equivariant to C_4 and C_2 are referred to as C_4 - and C_2 -equivariant, respectively. Rotations with smaller intervals are briefly discussed in the context of local isotropy in Section V C.

An important hyperparameter in equivariant CNNs is the group representation used in hidden layers.⁶⁰ This study adopted the regular representation of C_N , considering the following three reasons. First, the regular representation comprises all irreducible representations, that is, all minimal representations.^{61,62} Second, the CNNs using the regular representation have exhibited high accuracy in image classification.^{50–52,60} Third, each channel can be transformed nonlinearly and independently when the regular representation is used.^{50,60} In contrast, when the irreducible representation is employed, each channel cannot be transformed independently by a nonlinear function such as ReLU. A function such as Norm-ReLU⁶⁰ is necessary, as it acts to the vector norm and preserves the vector direction. A limitation such as in Norm-ReLU may reduce the expressive power of CNNs and may not be suitable for super-resolution. An example of the regular representation is presented in Appendix B.

Equivariant versions of DSC/MS and RRDN are referred to

as the Eq-DSC/MS and Eq-RRDN, respectively. The details of the Eq-DSC/MS and Eq-RRDN are described in Appendix A. These models were constructed by replacing usual convolution layers with the equivariant ones, while maintaining the number of channels to make the calculation time nearly the same. For instance, the regular representation of the C_4 group is composed of the 4 elements. If both input and output of a convolution layer have 64 channels, the C_4 -equivariant convolution employs 16 sets of the regular representation. In contrast to conventional kernels, the equivariant kernels are not completely independent over the spatial or channel dimension,⁶⁰ leading to a reduction in the number of trainable parameters. In general, there is a trade-off between expressive power and equivariance. Two examples of the trade-off are presented in Appendix B, along with a review of the equivariant convolution.

III. METHODOLOGY

This section presents the methods of training and testing the CNNs. The HR data were generated from the numerical simulations that solved the governing equations (Section III A). Whereas, the LR data were obtained by downsampling the HR data (Section III B). The supervised training was performed using the pairs of the HR and LR data (Section III C). The evaluation metrics are defined in Section III D. In addition to the above datasets, another dataset was utilized, where the data were generated separately from HR and LR simulations with the spectral nudging technique.^{72,73} The spectral nudging method is explained in Appendix C. The source code used in this study is available on the GitHub repository.⁷⁴

A. Fluid dynamics simulations

Two types of experiments were conducted: freely-decaying turbulence on a square flat torus and barotropic instability on a periodic channel. The governing equations for both experiments are as follows:

$$\frac{\partial \omega}{\partial t} + u \frac{\partial \omega}{\partial x} + v \frac{\partial \omega}{\partial y} = -v(-\Delta)^{n_v} \omega, \quad (5a)$$

$$(u, v) = \left(-\frac{\partial \psi}{\partial y}, \frac{\partial \psi}{\partial x} \right), \quad (5b)$$

$$\omega = \Delta \psi = \frac{\partial v}{\partial x} - \frac{\partial u}{\partial y}, \quad (5c)$$

where t denotes time, v is a positive real number, and n_v is a positive integer. The velocity components (u, v) are obtained using the stream function ψ in (5b), which is derived by solving the Poisson equation (5c) with the vorticity ω . For the two-dimensional translation and rotation, the vorticity is regarded as a scalar field, whereas the velocity is as a vector field. Large-scale flows in the ocean and atmosphere are described by similar equations⁷⁷ (i.e., quasi-geostrophic equations); the only difference is that the Poisson equation is three-dimensional and includes the altitude dimension.

The governing equations were numerically solved with the spectral method. A software library, ISPACK⁷⁸ coded with Fortran, was employed to perform spectral calculations. The discrete Fourier transform was used in a periodic direction, whereas the discrete sine/cosine transform was used in a direction bounded by two walls. In addition, the fourth-order Runge-Kutta method was utilized for the time integration.

The freely-decaying turbulence experiment was conducted following Fukami et al.²⁵ and Taira et al.⁷⁹ Here, $v = 10^{-2}$ and $n_v = 1$ were set, leading the governing equations (5) to the two-dimensional Navier-Stokes equations. The doubly periodic boundary condition was imposed on the flow domain $[0, 2\pi] \times [0, 2\pi]$. This domain, which is a square flat torus, has the rotational symmetry for multiples of 90° , although it is not isotropic. The grid numbers were set as 128×128 , which determined the truncation wavenumber of 42 for alias-free simulations. The initial condition was given at random with keeping the energy spectrum of $E(k) = a \times k \exp(-k^2/k_0^2)$, where k is the magnitude of wavenumber vector and $k_0 = 26.5$. The initial Reynolds number Re was controlled by the amplitude a : $Re \approx 80.0$ for the training data ($a = 9$) and $Re \approx 93.3$ for the test ($a = 12$), which were evaluated following Fukami et al.²⁵ Subsequently, on varying the random initial condition, 1,000 simulation sets were generated for the training and 100 simulations for the test. In each simulation, 10 snapshots were sampled between $1.1 \leq t \leq 2.0$ at intervals of 0.1. Thus, the training and test datasets comprise 10,000 and 1,000 snapshots, respectively. Test results similar to those shown below were obtained when the test data were halved, implying that the 1,000 snapshots are sufficient for estimating generalization errors.

Barotropic instability is a fundamental mechanism to make the evolution of flows complicated.⁷⁷ Here, $v = 10^{-30}$ and $n_v = 8$ were set, resulting in the governing equations (5) forming the two-dimensional Euler equations with the hyper-viscosity. The channel domain is $[0, 2\pi] \times [-\pi/2, \pi/2]$, where the x direction is periodic and the y direction is bounded by the two walls [$\psi = 0$ ($y = \pm\pi/2$)]. This domain exhibits the rotational symmetry for multiples of 180° and is clearly not isotropic. The grid size was set as 128×65 , which determined the truncation wavenumber of 42 for alias-free simulations. The initial condition was given by the superposition of an unstable laminar flow and random perturbations. The laminar flow has the shear region:

$$u = \begin{cases} U & \left(\frac{w}{2} \leq y \leq \frac{\pi}{2}\right), \\ U + 2U \frac{(y-\frac{w}{2})}{w} & \left(-\frac{w}{2} < y < \frac{w}{2}\right), \\ -U & \left(-\frac{\pi}{2} \leq y \leq -\frac{w}{2}\right), \end{cases} \quad (6)$$

where the shear is controlled by the width w and the speed U . The other component, i.e., the channel-wise velocity component v , is zero. The speed was set either $U = 0.25$ (positive shear) or -0.25 (negative shear). The number of experiments of $U = 0.25$ and -0.25 was kept the same. For the training data w was set to be 0.45 whereas for the test 0.40, which controlled the most unstable mode and resulted in the test data being slightly finer.⁷⁷ In the numerical experiments, the velocity profile (6) was made smooth around $y = \pm w/2$ to avoid the

initial discontinuity of the vortex field. As for the perturbations, each has the constant amplitude of 10^{-4} and a random phase. Subsequently, on varying the random phases, 800 and 80 simulations were generated for the training and test, respectively. In each simulation, 14 snapshots were sampled between $31 \leq t \leq 70$ at intervals of 3. Thus, the training and test datasets comprise 11,200 and 1,120 snapshots, respectively. Test results similar to those shown below were obtained when the test data were halved, implying that the 1,120 snapshots are sufficient to estimate generalization errors.

B. Data preparation

The HR snapshots of velocity or vorticity were generated from the fluid simulations in the previous subsection. The LR snapshots were obtained by downsampling the HR ones. Two downsampling algorithms were used: subsampling and local averaging. Subsampling implies the extraction of pixel values at certain intervals, which may be regarded as fluid observation such as particle image velocimetry (PIV).^{33,80} The local average can be used to compress HR fluid data and an SR model is then utilized to decompress the data.⁸¹

The subsampling and local averaging were processed in four steps. First, a scale factor s was determined. For instance, when $s = 2$, an LR image is twice as coarse as the HR image. Second, an HR snapshot of size $H \times W$ was resized to $H' \times W'$, where H' (W') was the multiple of s closest to H (W). Third, the downsampling algorithm was applied to the resized HR snapshot: in the subsampling, pixel values were extracted at intervals of $s \times s$; in the local average, each non-overlapping area of $s \times s$ was replaced with its mean. Fourth, the obtained snapshot of $H'/s \times W'/s$ was resized to $H \times W$. The bicubic interpolation⁸² was used in all cases of resizing mentioned above. Regarding the velocity, the algorithm was applied to u or v separately, because each component of vectors is added or subtracted independently in the Cartesian coordinates. The scale factor s was set to 5, 9, or 13 in Section IV and 4, 8, or 9 in Section V.

C. Training of CNNs

The CNNs were trained with supervised learning. They were implemented with PyTorch⁸³ 1.8.0 and e2cnn⁶⁰ 0.2.1. The latter is a software library for the equivariant deep learning of two-dimensional data.

An important hyperparameter of equivariant CNNs is the order N of a cyclic group C_N . For instance, when $N = 3$, a CNN is equivariant to the rotation in multiples of $360^\circ/3 = 120^\circ$. Here, $N = 4$ was set in the decaying turbulence and $N = 2$ in the barotropic instability experiment because the square torus possesses the rotational symmetry of 90° and the channel domain is symmetrical for the 180° rotation. Another important hyperparameter is the group representation. The regular representation was employed, as discussed in Section II B. Appendix D presents an investigation of the effect of changing several hyperparameters.

The Adam optimizer was used coupled with the loss function of mean squared error (MSE). The MSE is invariant to rotation and translation for scalars and vectors. The mini-batch size for the DSC/MS and Eq-DSC/MS was 100, while that for the RRDN and Eq-RRDN was 32. The learning rate was between 1.0×10^{-3} and 1.0×10^{-4} and was basically the same for the DSC/MS and Eq-DSC/MS and for the RRDN and Eq-RRDN. Each training was finished via early stopping with the patience parameter of 30 epochs, where the 30% of the training data was used for the validation.

Data augmentation was not employed because of the following two reasons. First, the data augmentation is not necessary to equivariant CNNs because they exhibit symmetries as the prior knowledge regardless of training.⁵⁸⁻⁶⁰ Second, the data augmentation may impose inappropriate symmetries that the original data do not possess (Section V A). Without the data augmentation, the comparison between the non-equivariant and equivariant CNNs is clarified and the symmetry inherent in the original data becomes distinct.

D. Evaluation metrics of CNNs

The following three metrics were utilized to evaluate the CNNs: norm error ratio, energy spectral error, and equivariance error ratio.

The norm error ratio (NER)²⁵ is defined as follows:

$$NER = \frac{\sum_{\text{space}} \|Y - \hat{Y}\|}{\sum_{\text{space}} \|Y\|}. \quad (7)$$

The summation is taken over the entire space. The symbol $\|\cdot\|$ denotes the Euclidean norm when the inference \hat{Y} and ground truth Y are vectors, whereas it is the absolute value in the case of scalars. In the actual evaluation, the NER (7) was averaged over the entire test sample.

The energy spectral error (ESE) was introduced to evaluate the validity of spatial patterns by Wang et al.¹⁴ The NER is invariant against any pixel shuffling, indicating that it does not necessarily reflect the consistency of spatial patterns. The ESE is equal to the root-mean-squared error of the logarithm of the energy spectra between the inference and ground truth:

$$ESE = \sqrt{\frac{1}{M} \sum_{\text{samples}, k} [\log E(k) - \log \hat{E}(k)]^2}, \quad (8)$$

where E (\hat{E}) is the energy spectrum of the ground truth (inference), M is the normalization constant for the mean, and the summation is taken over the wavenumber and the entire test sample. The ESE is interpreted as the error of spatial correlations through the convolution theorem.

Wang et al.¹⁴ also introduced the equivariance error, which measures the equivariance of any model and is calculated without referring to the ground truth. The equivariance error ratio (EER) is defined by

$$EER := \frac{\sum_{\text{central region}} \|(f \circ g)(X_{\text{in}}) - (g \circ f)(X_{\text{in}})\|}{\sum_{\text{central region}} \|(g \circ f)(X_{\text{in}})\|}, \quad (9)$$

where f denotes a CNN and g is a representation of translation or rotation (3). The summation is taken over the central 48×48 pixels to avoid the effect of extrapolation such as zero padding. In the actual evaluation, the EER (9) was averaged over the entire input sample. Only the rotational transformation is considered below because conventional CNNs are equivariant to translation and the usefulness of CNNs in super-resolution has been confirmed by many studies (Section I).

IV. RESULTS

This section presents an evaluation of the equivariant and non-equivariant CNNs using the metrics in the previous subsection. Only the results of SR of velocity are presented owing to similar results in case of vorticity. Appendix D 4 compares the SR of velocity and vorticity.

A. Freely-decaying turbulence experiment

Figure 2 shows an example of the vorticity calculated from the super-resolved velocity, where the scale factor $s = 9$. The finite difference operation in deriving the vorticity enhances the small-scale structure in the super-resolved flow. Regarding the baseline of bicubic interpolation, the shape of each vortex is ambiguous and the difference from the ground truth is large. All SR models reproduce well the small-scale structure, regardless of the equivariance and non-equivariance.

Figure 3 compares the NERs and ESEs from the locally averaged and subsampled velocity. With increasing scale factor s , the errors tend to be increased. The NER and ESE values of the Eq-DSC/MS and Eq-RRDN are comparable to those of the DSC/MS and RRDN in all cases, respectively. The Eq-RRDN and RRDN tend to show slightly lower errors than the Eq-DSC/MS and DSC/MS, which is likely due to the Eq-RRDN and RRDN being deeper and having more parameters (Table I).

Table I compares the numbers of the trainable parameters in the SR models. The number of parameters is generally smaller in equivariant models than in non-equivariant ones owing to the constraint of the equivariance (Appendix B). The C_4 -equivariant models have fewer parameters than the C_2 -equivariant ones (Table I) because the C_4 group contains C_2 and the constraint on the C_4 equivariance is stricter. The reduction in parameters implies that the expressive power of the equivariant SR models is lower in principle; however, the Eq-DSC/MS and Eq-RRDN exhibit comparable performance with the DSC/MS and RRDN, respectively (Figs. 2 and 3). This result indicates that imposing the equivariance does not necessarily result in the deterioration of the accuracy of super-resolution. The smaller number of parameters suggests that an equivariant model is trainable with a smaller size of data.¹⁶ This suggestion is confirmed in Appendix D 2.

Figure 4 shows the EER against the rotation angle. The subsampled velocity with the scale factor $s = 9$ was super-resolved; similar figures were obtained in the other cases. The

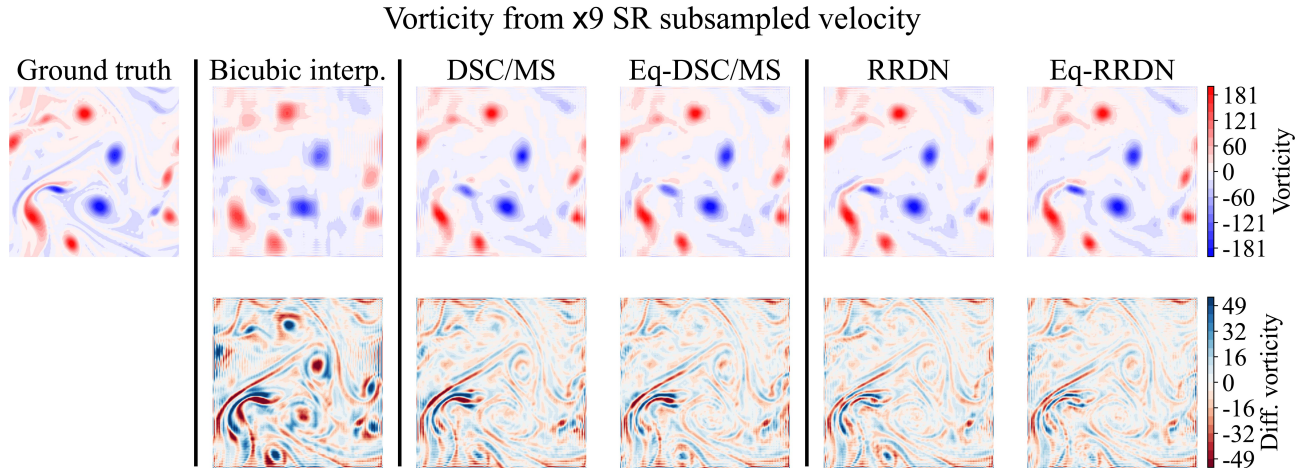
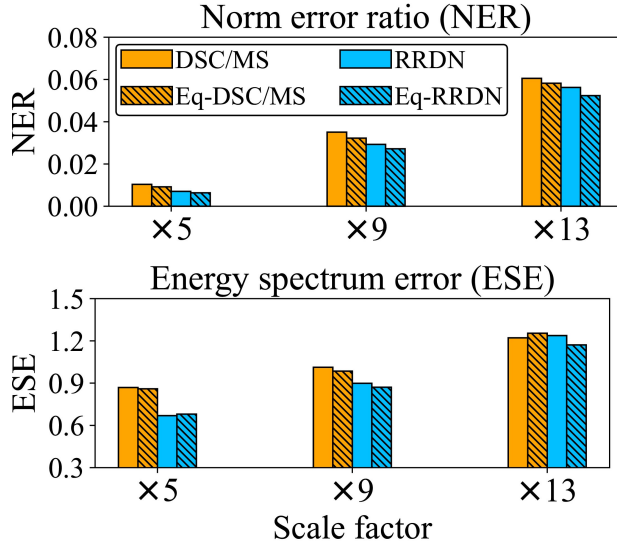


FIG. 2. An example of the vorticity calculated from the super-resolved velocity in the decaying turbulence experiment. The scale factor s is nine, that is, the super-resolution increases the resolution by a factor of nine. The subsampled velocity was used as input. The label of “Bicubic interp.” means bicubic interpolation. The bottom row shows the difference from the ground truth.

SR of locally averaged velocity



SR of subsampled velocity

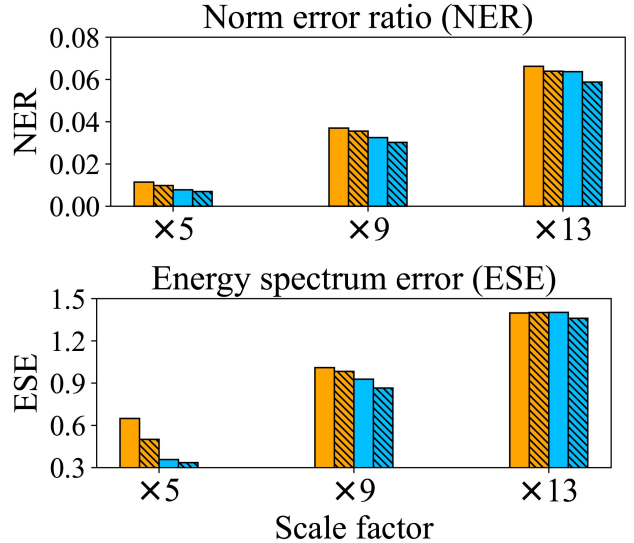


FIG. 3. Test scores calculated from the locally averaged and subsampled velocity in the decaying turbulence experiment. The norm error ratio (NER) in (7) reflects pixel-wise errors. The energy spectrum error (ESE) in (8) reflects spatial pattern errors.

TABLE I. Numbers of the trainable parameters in the super-resolution models. The C_4 -equivariant DSC/MS and RRDN are used in the decaying turbulence experiment (Section IV A) and the C_2 -equivariant ones are used in the barotropic instability experiment (Section IV B).

Model name	Number of trainable parameters
DSC/MS	141,298
C_2 -Equivariant DSC/MS	37,128
C_4 -Equivariant DSC/MS	18,564
RRDN	1,256,770
C_2 -Equivariant RRDN	419,104
C_4 -Equivariant RRDN	209,552

square flat torus possesses the rotational symmetry for multiples of 90° , and a rotated flow is a solution of the governing equations (5). Thus, an SR model should be equivariant to the rotation by multiples of 90° (i.e., C_4 -equivariant). The original models (DSC/MS and RRDN) show smaller EERs at the multiples of 90° than those at the other angles, implying that the conventional CNNs learn the approximate C_4 equivariance (Fig. 4). However, the magnitude of EERs is not sufficiently low, compared to that of the equivariant models (Eq-DSC/MS and Eq-RRDN). Whereas, at the rotation angles other than the multiples of 90° , the magnitude of EERs is nearly the same for the equivariant and original models (Fig. 4) because the C_4 -equivariance does not guarantee the equivariance to the other

angles.

Equivariance should be explicitly incorporated into neural network designs as the prior knowledge provided symmetries of a physics system are clear and the data inherit the symmetries. Although conventional CNNs can learn the equivariance from data, a larger size of data or data augmentation may be necessary. Equivariance as the prior knowledge results in a reduction of the number of learnable parameters, and the model can be trained with a smaller size of data. This trainability is important in fluid mechanics because the computational cost of fluid simulations is often high and the sufficient size of data may not be available.

B. Barotropic instability experiment

The results of the barotropic instability experiment are briefly described below. The results are similar to those of the decaying turbulence. The C_2 -equivariant CNNs were used because the channel domain is symmetrical to the 180° rotation.

Figure 5 shows an example of the vorticity calculated from the super-resolved velocity. The vortices obtained with the bicubic interpolation have indistinct shapes. In contrast, the SR models reproduce well the cat's eye structure⁷⁷ associated with the collapse of the laminar flow having the strong shear region. The flows inferred by the equivariant models are nearly the same as those by the non-equivariant ones.

Figure 6 compares the NERs and ESEs from the locally averaged and subsampled velocity. The figure suggests that the Eq-DSC/MS and Eq-RRDN are as accurate as the DSC/MS and RRDN, respectively. The Eq-RRDN and RRDN tend to exhibit lower errors than the Eq-DSC/MS and DSC/MS as in the case of the decaying turbulence (Fig. 3).

Figure 7 shows the EER against the rotation angle. The subsampled velocity with the scale factor $s = 9$ was super-resolved; similar figures were obtained in the other cases. The channel domain possesses the rotational symmetry of 180° . Thus, an SR model should be equivariant to the 180° rotation (i.e., C_2 -equivariant). Although the original models (DSC/MS and RRDN) learn the approximate C_2 equivariance, the EERs at 180° are not sufficiently low, compared to those of the equivariant ones (Eq-DSC/MS and Eq-RRDN). At the other rotation angles, the magnitude of EERs is nearly the same for the equivariant and original models (Fig. 7).

V. DISCUSSIONS

This section demonstrates that the equivariance may be broken owing to the method of data generation or the choice of input data regardless of the symmetry of fluid systems. If the equivariance between the input and output is broken, the super-resolved velocity cannot be regarded as a geometric vector field. In this case, conventional CNNs should be used, in which vector is treated as a quantity having no direction.

Section VA demonstrates that the equivariance can be broken by the data generation of subsampling. Section

VB discusses an experiment using the spectral nudging technique.^{72,73} The data generated by the spectral nudging preserve the symmetry intrinsic to the governing equations (Appendix C). However, this symmetry can be broken depending on the choice of input data. The equivariance to local rotation is discussed in Section VC. This local equivariance is referred to as the gauge equivariance.^{11,84,85}

A. A data generation breaking the equivariance

The C_4 -equivariance has been imposed on the DSC/MS and RRDN in the decaying turbulence experiment because both flow domain and governing equations possess the rotational symmetry for multiples of 90° . The original DSC/MS and RRDN learned the approximate C_4 -equivariance from the training data (Fig. 4), implying that the data themselves inherit the rotational symmetry from the flow domain and governing equations. However, this symmetry can be broken, depending on the method of data generation.

Figure 8 is a schematic that compares the subsampling of the scale factor $s = 2$ and 3. The LR image for $s = 2$, generated by subsampling, is varied via the orientation of the HR image, whereas the LR image for $s = 3$ is not. In the former case, the local correspondence between LR and HR patterns depends on the orientation. Mathematically, the subsampling of an even number s is not commutative with the rotation in multiples of 90° . This statement is formulated by

$$(d \circ g)(Y) \neq (g \circ d)(Y), \quad (10)$$

where d is the subsampling operation, g is the representation of rotation by multiples of 90° [Eq. (3)], and Y is an HR velocity field. Note that the input LR field is given by $X = d(Y)$.

The C_4 -equivariance is broken by the non-commutativity of subsampling (10). Consider an HR velocity Y and its rotated version $g(Y)$, both of which can exist because the flow domain and governing equations have the rotational symmetry. The LR fields are generated as $X = d(Y)$ and $X' = d(g(Y))$. Importantly, X' is not equal to $g(X)$ [$= g(d(Y))$]. The non-commutativity results in the inconsistency of LR and HR pairs. When an SR model is trained with the pairs of (X, Y) and $(X', g(Y))$, it fails to learn the equivariance because $(X', g(Y))$ is not $(g(X), g(Y))$. Thus, in this case, the C_4 -equivariance should not be imposed on the SR model.

The effect of the non-commutativity (10) is demonstrated through comparisons of the super-resolved velocity of the decaying turbulence for $s = 8$ and 9 (Fig. 9). The NERs of the equivariant models are much greater than those of the non-equivariant models, only in the case of subsampling of $s = 8$. In contrast, when $s = 9$ the subsampling is commutative with the rotation, and such large errors are not observed. As for the local average, the operation is always commutative with the rotation regardless of s , and large errors are not found in both cases of $s = 8$ and 9 (Fig. 9). The result implies that the SR model deteriorates if the equivariance is forcefully imposed when the data do not have the rotational symmetry. In

Equivariance error ratio (EER): $\times 9$ SR of subsampled velocity

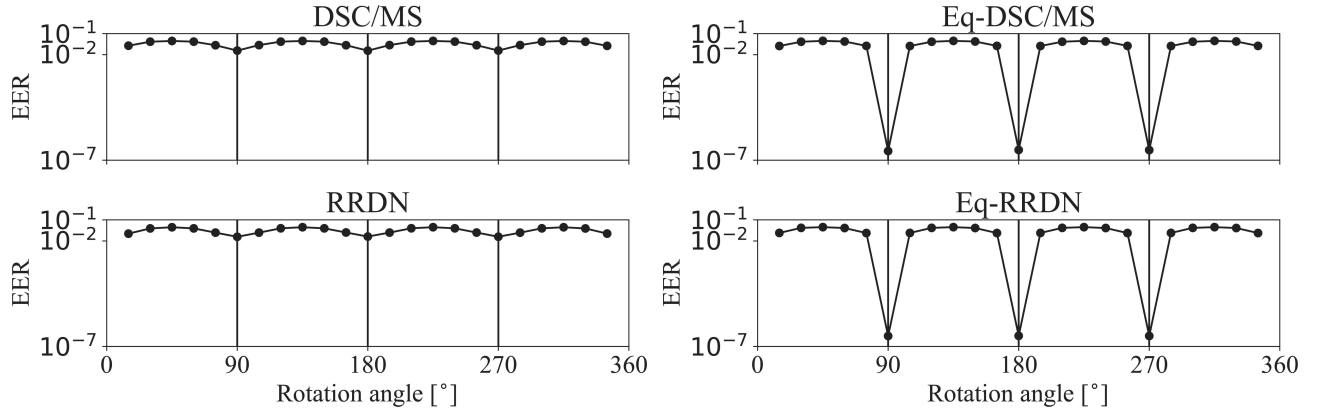


FIG. 4. Equivariance error ratio (EER) against the rotation angle calculated with the super-resolution models of velocity in the decaying turbulence experiment. The EER is defined in (9). The scale factor was nine and the low-resolution data were generated by subsampling. The rotation angle interval is 15° , where 0° and 360° are omitted.

Vorticity from $\times 9$ SR subsampled velocity

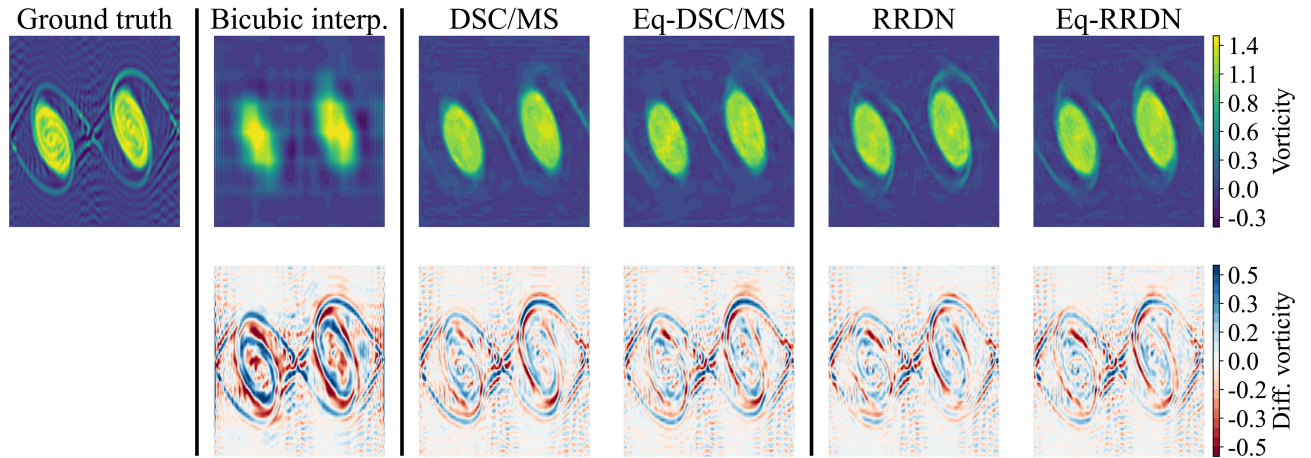


FIG. 5. An example of the vorticity calculated from the super-resolved velocity in the barotropic instability experiment. The scale factor s is nine, that is, the super-resolution models make the resolution nine times finer. The subsampled velocity was used as input. The label of “Bicubic interp.” means bicubic interpolation. The bottom row shows the difference from the ground truth.

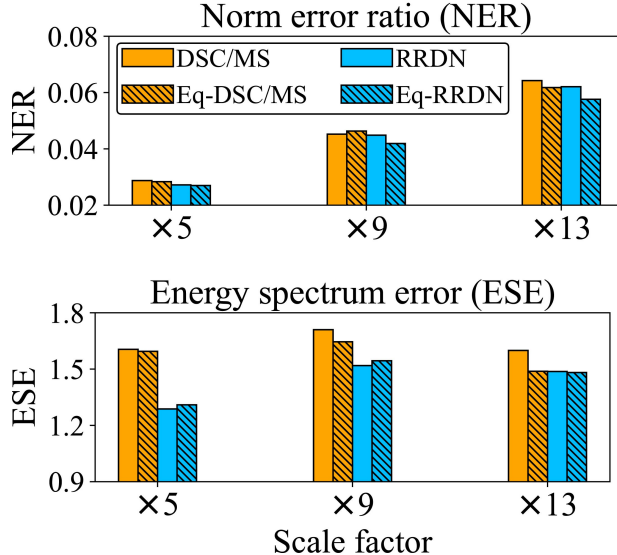
contrast to the NER, the ESEs in Fig. 9 are comparable between the equivariant and non-equivariant models even for the subsampling of $s = 8$. The non-commutativity of subsampling largely affects pixel-wise values but not spatial patterns.

Figure 10 shows the EER curves for the non-equivariant models (DSC/MS and RRDN) with $s = 8$ and 9. In the case of the local average, the models learn the approximate C_4 -equivariance regardless of s . In contrast, in the case of subsampling, the C_4 -equivariance is learned when $s = 9$ (solid curves) although not when $s = 8$ (dashed curves). The result indicates that the data do not have the equivariance in the latter case.

Even if a flow domain and governing equations have rotational symmetry, the symmetry may not carry over to LR and HR velocity fields. An SR model trained with these inconsistent data is not equivariant. If the coordinates are rotated

(i.e., a passive transform), both LR and HR velocities are rotated. However, as the SR model is not equivariant, the super-resolved velocity is not rotated according to the rotation of the input. Consequently, the output velocity does not satisfy the covariance to rotation and cannot be regarded as a geometric vector. In this case, the conventional CNNs should be used, in which vector is treated as a quantity having no direction. In other words, the conventional CNNs should be applied to data with a fixed orientation because the data themselves do not exhibit the rotational symmetry. As only the transformation of translation is permitted, it is impossible to distinguish between data of scalars and vectors on the Cartesian coordinates. The data augmentation using rotations should not be employed because it changes the orientation of the data and imposes the inappropriate symmetry of rotation that the original data do not possess.

SR of locally averaged velocity



SR of subsampled velocity

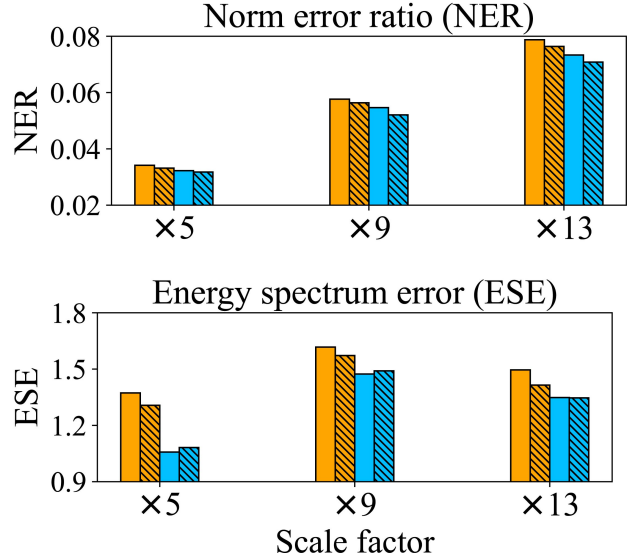


FIG. 6. Test scores calculated from the locally averaged and subsampled velocity in the barotropic instability experiment. The norm error ratio (NER) in (7) reflects pixel-wise errors. The energy spectrum error (ESE) in (8) reflects spatial pattern errors.

Equivariance error ratio (EER): $\times 9$ SR of subsampled velocity

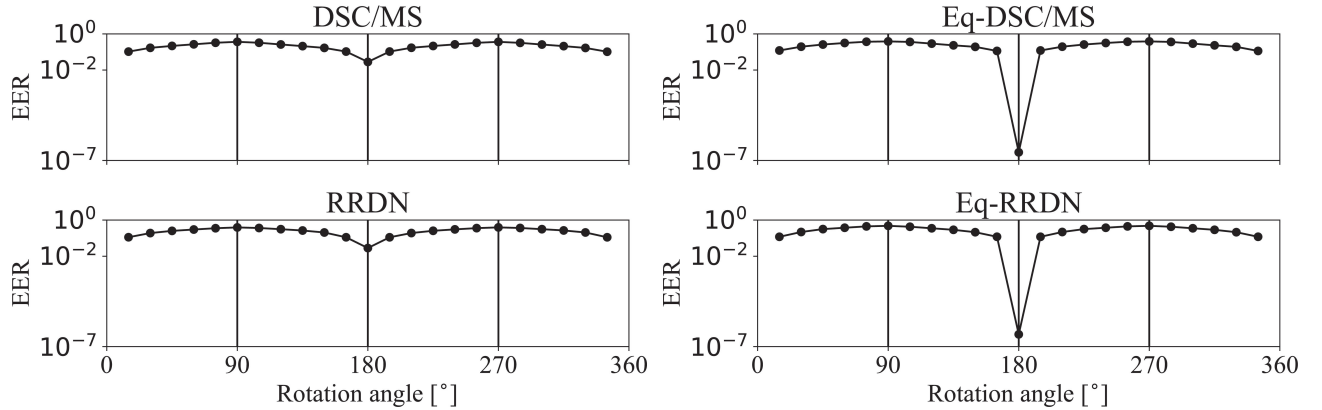


FIG. 7. Equivariance error ratio (EER) against the rotation angle calculated with the super-resolution models of velocity in the barotropic instability experiment. The EER is defined in (9). The scale factor was nine and the low-resolution data were generated by subsampling. The rotation angle interval is 15° , where 0° and 360° are omitted.

B. An input choice breaking the equivariance

This subsection discusses that the equivariance can be broken depending on the choice of input data. The SR models are applied to the data generated with the spectral nudging method.^{72,73} Appendix C presents the details on the spectral nudging technique used in this study.

Both LR and HR data are generated from the fluid simulations in an experiment using the spectral nudging. The LR data are generated by numerically solving the governing equations (5). In the case of the HR simulation, a linear relaxation toward the LR flow is added to the right-hand side of (5a). If the relaxation time is sufficiently small, the large-scale flow

pattern in the HR simulation becomes similar to that in the LR one. In addition to the large scales, the small-scale motions evolve in the HR simulation according to the governing equation (5a), where the relaxation term vanishes because these small scales are not resolved in the LR model. The spectral nudging technique^{72,73} is understood as a method of dynamical downscaling that reproduces fine-scale motions not resolved in LR simulations.

The spectral nudging may aid in constructing a super-resolution simulation system.⁴⁵ The purpose of this system is to reduce the computational cost of HR simulations. After training an SR model, that is, at the inference stage, only the LR fluid simulation is conducted and the HR results are ob-

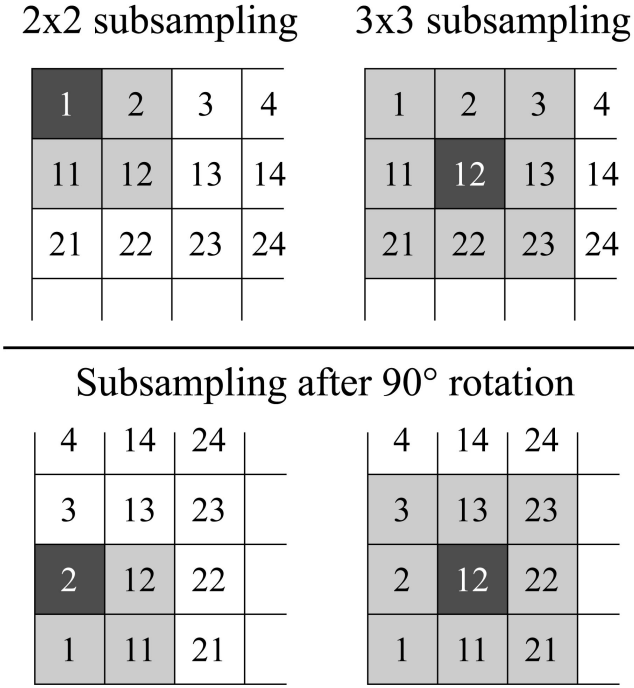


FIG. 8. Schematic showing the commutative property of subsampling with rotation. In the case of the scale factor $s = 2$, the subsampling picks up the values from the upper left pixels (black tiles) in the windows of 2×2 . When $s = 3$, the subsampling extracts the central pixels (black tiles) of the windows regardless of the orientation.

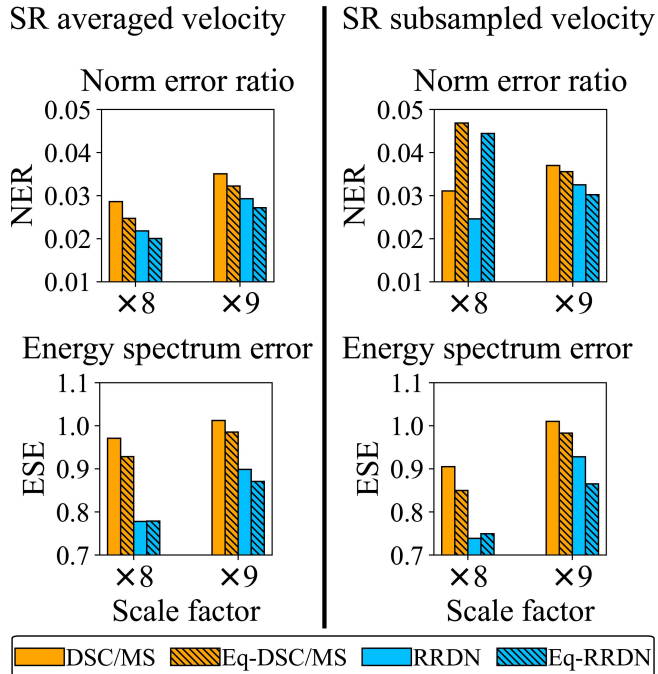


FIG. 9. Test scores calculated from the locally averaged and subsampled velocity in the decaying turbulence experiment. The norm error ratio (NER) in (7) reflects pixel-wise errors. The energy spectrum error (ESE) in (8) reflects spatial pattern errors. All scores of $s = 9$ are the same as those in Fig. 3 and are shown again to compare with the values of $s = 8$.

tained by feeding the LR snapshots to the SR model. Thus, a dataset generated with the spectral nudging can be utilized to train an SR model in the super-resolution simulation system.

The spectral nudging method was applied to the case of barotropic instability, which is more appropriate than the decaying turbulence because the initial laminar flow is clearly developed into smaller scales. The truncation wavenumber of the LR fluid model was 10 and that of HR was 42; the scale factor s was regarded as 4. For comparison, another set of LR data was generated by locally averaging the HR flows obtained from the simulations with the spectral nudging. The value of s was 4 for the local average.

Figure 11 shows an example of the vorticity calculated from the super-resolved velocity. The non-equivariant models (DSC/MS and RRDN) reproduce the small-scale pattern in both cases of local averaging and spectral nudging. In contrast, the super-resolved flows inferred by the equivariant models (Eq-DSC/MS and Eq-RRDN) are clear in the local average, although blurred in the spectral nudging.

Figure 12 shows the NERs and ESEs in the cases of local averaging and spectral nudging. The errors tend to be larger in the spectral nudging than those in the local average, which is attributed to the HR signals not being completely contained in the LR data of the spectral nudging. In the case of local average, the NERs and ESEs of the equivariant models are comparable to those of the non-equivariant ones, as in Fig. 6. Whereas, in the case of spectral nudging, the NERs and ESEs of the equivariant models are larger than those of the non-equivariant ones (Fig. 12).

The LR and HR velocities from the fluid simulations with the spectral nudging have the 180° rotational symmetry because the channel domain and governing equations have this symmetry even when the linear relaxation is added in the HR fluid model (Appendices C 1 and C 2). In other words, a set of LR and HR velocities rotated by 180° is a solution to the governing equations and can be obtained from the rotated initial condition. Moreover, the LR velocity generated with the local average inherits the rotational symmetry because the average operation is commutative with the 180° rotation (Section V A). Therefore, in both cases, an SR model should be C_2 -equivariant.

Figure 13 shows the EER curves of the non-equivariant models (DSC/MS and RRDN). The decrease in the EER at 180° is observed in the local average. In contrast, the EER is the largest at approximately 180° in the spectral nudging. The SR models learn the C_2 -equivariance only in the case of the local average. This result was confirmed even when the training data size was doubled, indicating that the result is not due to the lack of training data. The large NERs and ESEs of the equivariant models (Eq-DSC/MS and Eq-RRDN) in the spectral nudging (Fig. 12) can be attributed to the equivariance being forcefully imposed although the velocity data do not have the 180° rotational symmetry.

The result of the spectral nudging appears to contradict the fact that the velocity rotated by 180° is a solution to the governing equations. A possible reason is that the choice of input data was inappropriate and broke the equivariance. This reason is explained using a graphical model of the LR and HR ve-

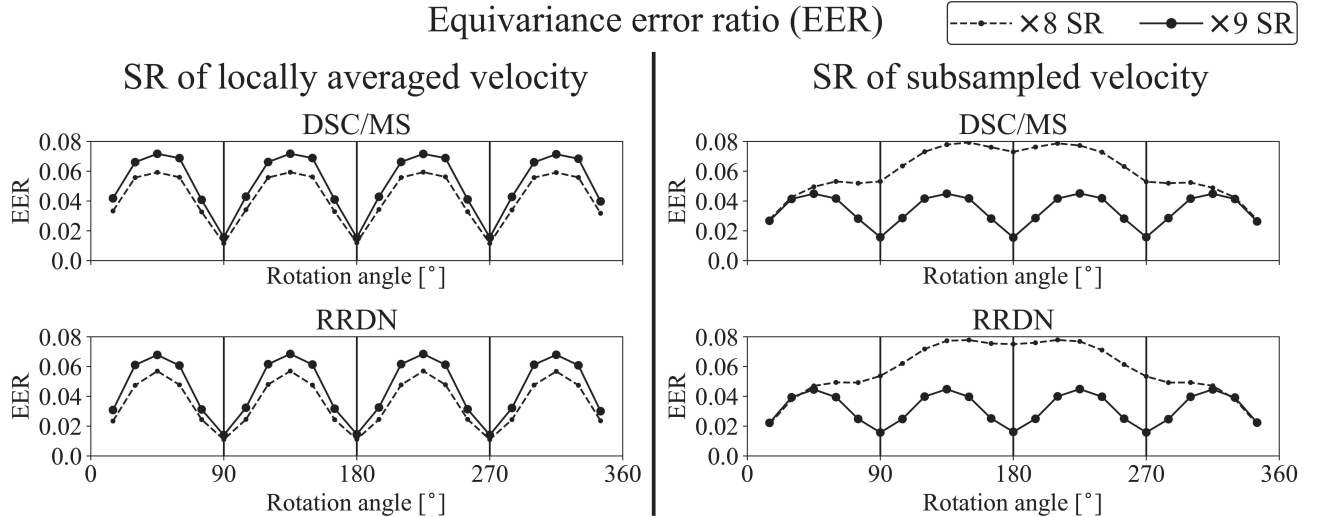


FIG. 10. Equivariance error ratio (EER) against the rotation angle for the non-equivariant super-resolution model of velocity (DSC/MS and RRDN) in the decaying turbulence experiment. The EER is defined in (9). The scale factor s is eight or nine. The interval of rotation angle is 15° , where 0° and 360° are omitted.

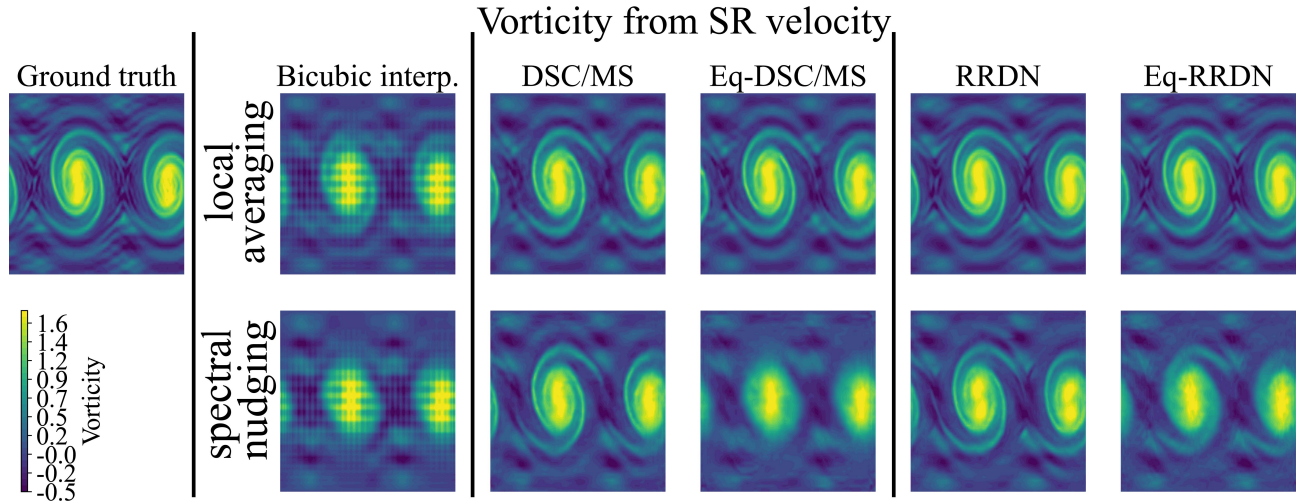


FIG. 11. An example of the vorticity calculated from the super-resolved velocity in the barotropic instability experiment. The upper figures are from the case of local averaging and the bottom from the case of spectral nudging. The label of “Bicubic interp.” means bicubic interpolation.

locities (Fig. 14). The governing equations satisfy the Markov property, regardless of the linear relaxation being added (Appendix C 1). The HR velocity v_n^H at $t = n$ depends on v_{n-1}^H as well as the LR velocity v_{n-1}^L through the relaxation term.

Consider the problem of inferring the HR velocity v_n^H . We first discuss the case where only the LR velocity v_n^L is utilized as in the above experiment (Figs. 11 - 13), although v_n^H depends on the past states. The past LR velocities v_t^L ($t < n$) are regarded as unobserved because these velocities are not fed into an inference model. When v_n^L was rotated by 180° , it is not clear whether all past velocities v_t^L ($t < n$) are rotated or not. This unclarity suggests that the model is challenging to learn the equivariance from the training data. Moreover, the graphical model indicates that v_n^H is conditionally independent of the current and future LR velocities $[v_t^L (t \geq n)]$ when

the previous LR state v_{n-1}^L is provided.

The usage of past states is consistent with the graphical model (Fig. 14) because the current HR velocity v_n^H depends on all past LR velocities v_t^L ($t < n$). A neural network considering the structure of the graphical model is necessary because the number of past time steps required to infer the current state is not clear and may depend on the history of the LR and HR states. Interestingly, the current HR velocity is conditionally independent of the future LR ones, which is different from a situation where the Kalman smoother is applied. The previous studies^{29,31,46} successfully reconstructed HR flow fields by utilizing time series of LR fields. When a time series is used as input, the Galilean equivariance^{14,71} should be incorporated as well as the equivariance to rotation and translation.

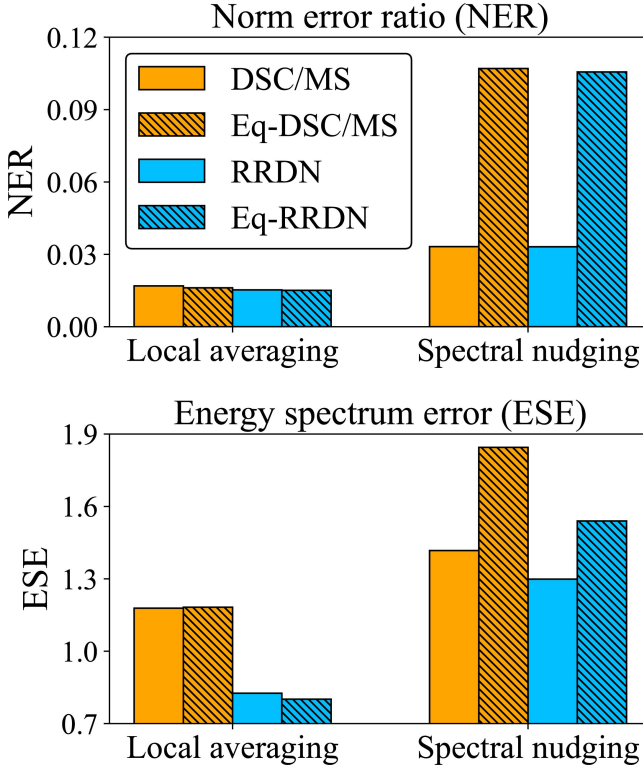


FIG. 12. Test scores in the barotropic instability experiment. The datasets used here were generated with the local averaging and spectral nudging. The norm error ratio (NER) in (7) reflects pixel-wise errors. The energy spectrum error (ESE) in (8) reflects spatial pattern errors.

C. Equivariance to local rotation

The global equivariance has been discussed till now. This subsection focuses on the equivariance to local rotation, which is a type of gauge equivariance.^{84,85} In the local rotation, the rotation angle can depend on the position. Here the gauge transformation is defined as a local change in basis vectors and is more general than local rotation.

Three things can be mentioned to motivate the discussion on the gauge equivariance. First, the gauge equivariance extends the application of super-resolution. If an SR model is equivariant to local rotation, the model can be applied to cropped data in any orientation without compromising on the accuracy and physical validity. Second, if a convolution operation is globally equivariant to certain combinations of rotation and translation, it is also locally equivariant and vice versa.⁶⁰ This implies that the C_4 -equivariant models used above (Eq-DSC/MS and Eq-RRDN) are equivariant to the global and local rotation in multiples of 90° . Third, SR models with the convolution often utilize the local correspondence between LR and HR patches. The locality can be interpreted with the sparse-coding-based method, which can be realized by CNNs.¹⁹ Moreover, even if a model can learn the non-locality,^{86–88} the convolution layer is often employed as a part of the non-local models.

The locality in two-dimensional fluids is discussed from a

physics perspective. Two-dimensional fluid is a long-range interacting system,⁸⁹ where any local change can affect globally. This non-locality can be understood from the fact that the stream function and vorticity are linked by the Poisson equation. Even on the infinite plane, the Green function is proportional to the logarithm. Similarly, large-scale flows in the ocean and atmosphere at mid-and high-latitudes exhibit non-locality because of the three-dimensional Poisson equation of the quasi-geostrophic system.^{77,89} Therefore, the super-resolution does not rigorously satisfy the local equivariance for these fluids. For instance, when a vortex shape is distorted locally in an LR field, the super-resolved flow is globally affected.

CNNs have succeeded in super-resolving two-dimensional fluids^{24–30} and large-scale flows in the ocean and atmosphere.^{41,43,44,46,47} In these studies, quite deep models are not always used. Those results suggest that the long-range interacting nature is not critical to the super-resolution in practice, and the gauge equivariant CNNs^{84,85} may be useful for the fluid SR. When applying a gauge equivariant CNN, it may be natural to assume the local isotropy even if the entire domain is not globally isotropic. The results of Figs. 4 and 7 suggest that the local symmetry may become indistinct due to the global one. These figures show the EERs evaluated over the local patch around the center and indicate that the non-equivariant SR models (DSC/MS and RRDN) learn the approximate equivariance from the training data. The EERs are minimal at the rotation angles reflecting the global symmetries, and the local isotropy is not clear in Figs. 4 and 7. Thus, to investigate the effectiveness of gauge equivariant CNNs, it may be necessary to apply an SR model to complex flows where global symmetries are not obvious, such as atmospheric flows.

VI. CONCLUSIONS

Vector is an essential quantity in physics. In applications of convolutional neural networks (CNNs), vectors are often apparently processed as quantities having no direction such as colors in images. This study investigated the effect of treating vector as a geometrical quantity, wherein a direction was recognized in terms of super-resolution (SR) of two-dimensional flows. Vector can be distinguished from scalar by the transformation law, that is, the covariance in geometry.^{8,9} Equivariant CNNs^{50,58–60} can incorporate the transformation laws as the prior knowledge and preserve the covariance of vector regardless of training. In this study, two existing non-equivariant CNNs^{25,32} were converted into equivariant ones using a theory of equivariant deep learning,⁶⁰ where the rotation and translation equivariance were considered. Further, to generate the training data, the two-dimensional fluid simulations were conducted and the pairs of low- and high-resolution (LR and HR) velocities were generated. Two types of data were used: in the first type, the LR data were generated by downsampling the HR ones; in the other, both LR and HR data were generated from the numerical simulations with the spectral nudging method.^{72,73}

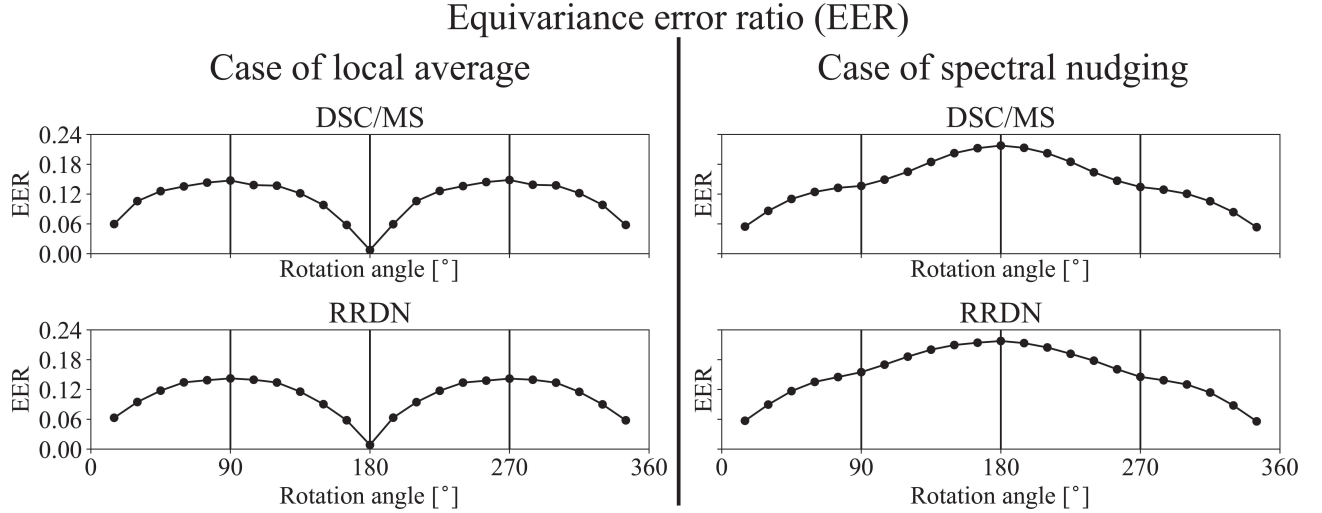


FIG. 13. Equivariance error ratio (EER) against the rotation angle calculated with the non-equivariant super-resolution models of velocity in the barotropic instability experiment. The EER is defined in (9). The low-resolution velocity was generated with (left) the local average and (right) the spectral nudging. The rotation angle interval is 15° , where 0° and 360° are omitted.

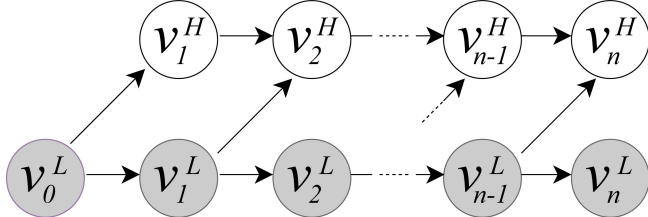


FIG. 14. Graphical model of the velocity governed by the equations with the spectral nudging [Eqs. (C3) and (C4)]. The superscript H (L) denotes the high- (low-) resolution. The subscript represents the time index. The circles of the low-resolution states are colored gray because they are observed at the inference step.

The contrasting results were obtained depending on the symmetry of the data. When the data inherited the rotational symmetry from the flow domain and governing equations, the equivariant CNNs exhibited comparable accuracy with the non-equivariant ones. As the number of learnable parameters is smaller in the equivariant CNNs, these models can be trained with a smaller size of the data. This trainability is important in fluid mechanics because the computational cost of fluid simulations is often high and the sufficient size of data may not be available. Therefore, when a dataset possesses rotational symmetry, the transformation law of vector should be incorporated into a neural network design as the prior knowledge, where vector is treated as a quantity having direction.

Further, it was confirmed that the symmetry of the data can be broken. This was demonstrated through two examples. In the first case, the method of data generation (i.e., subsampling) rendered the correspondence between LR and HR patterns dependent on the orientation, thereby breaking the equivariance of SR. In the second case, the choice of input data was not appropriate in the experiment with the spectral nudging. Although the HR velocity depended on all past LR

states, only the current LR velocity was fed into the CNNs. This insufficient input might have broken the equivariance of SR. When an existing dataset does not reflect the rotational symmetry of the governing equations, the accuracy of a CNN may deteriorate if the equivariance is forcefully imposed. In this case, the conventional CNNs should be used, in which vector is treated as a quantity having no direction.

There are at least three directions to future work. The first is the SR of more complicated data. The present study utilized the Cartesian coordinates, where each component of vectors is added independently due to the orthonormal basis. Three-dimensional oceanic or atmospheric flows may be appropriate because latitudes and longitudes compose irregular grids and these grids are often used to describe those data. The second is the incorporation of other equivariance. The Galilean^{14,71} or scale equivariance^{14,57} is an important symmetry of fluid systems. The third is the SR of time-series data.^{29,31,46} The input of time series may be essential to super-resolve flows in which the LR and HR data are separately generated as in the experiment of spectral nudging.

ACKNOWLEDGMENTS

This work was supported by the JSPS KAKENHI (grant number 20H05751). The deep learning was conducted on the supercomputer of TSUBAME 3.0 at the Tokyo Institute of Technology. We would like to thank Editage (www.editage.com) for English language editing.

DATA AVAILABILITY STATEMENT

The data that support the findings of this study are available within the article. The source code is available on the GitHub repository.⁷⁴

Appendix A: Implementation of the equivariant CNNs

This section presents the details on the implementation of the equivariant CNNs. Two existing CNNs were made equivariant: the hybrid DSC/MS model by Fukami et al.²⁵ and the RRDN by Bode et al.³² The architectures of the DSC/MS and RRDN are shown in Figs. 15 and 16, respectively. The input of both models is a snapshot of either velocity or vorticity and the output is the super-resolved field at the instantaneous time.

If each layer is equivariant, the entire network is equivariant.^{11,60} Each layer in the DSC/MS and RRDN was made equivariant as follows. A two-dimensional convolution layer was replaced with the equivariant convolution.⁶⁰ A max-pooling layer was replaced with the norm max-pooling^{52,60} when the input was a vector field, while it remained unchanged when the input was scalar or described by the regular representation. In all cases, the pooling operation is equivariant.^{50,52,60} Further, the linear or bicubic interpolation was used in resizing data, both of which are equivariant because the weights of interpolation depend only on the absolute difference in x or y coordinates.⁸² The skip connection is equivariant because it is an addition operation between features having the same type.¹⁴ Because all hidden layers utilize the regular representation (Section II B), a channel-wise non-linear transformation such as ReLU is equivariant.^{50,60}

The representation of the input or output of the entire network was determined as follows.⁶⁰ When the input or output was scalar, it was regarded as a feature field with the trivial representation,^{61,62} wherein any conversion was not necessary. A vector field was naturally considered as a feature with the irreducible representation of order 1.^{61,62}

All the CNNs used in the present study were implemented with PyTorch⁸³ and e2cnn.⁶⁰ The source code is available on the GitHub repository.⁷⁴

Appendix B: Review on equivariant convolution

This section reviews the equivariant convolution.^{50,53,59,60,63} The aim is to explain a trade-off between the expressive power and equivariance, but not present the details on the theory. We discuss a linear constraint that is satisfied by equivariant kernels and subsequently present two examples to understand the meaning of the constraint.

1. Linear constraint on equivariant kernels

The convolution is defined by

$$F_{\text{out}}(\mathbf{y}) = \kappa * F_{\text{in}} = \int \kappa(\mathbf{y} - \mathbf{x}) F_{\text{in}}(\mathbf{x}) d\mathbf{x}, \quad (\text{B1})$$

where $*$ stands for the convolution, the input F_{in} and output F_{out} are tensors generally having different ranks, κ is a kernel, and the integral is performed over the continuous Euclidean plane without boundary. The multiplication between κ and F_{in} is generally a matrix operation. Consider that the input F_{in}

and output F_{out} are transformed by the action of an element of the special Euclidean group $SE(2)$ as in Eq. (3):

$$g_{\text{in}} : F_{\text{in}}(\mathbf{x}) \mapsto \pi_{\text{in}}(\rho) F_{\text{in}}(\rho^{-1}(\mathbf{x} - \mathbf{t})), \quad (\text{B2})$$

$$g_{\text{out}} : F_{\text{out}}(\mathbf{x}) \mapsto \pi_{\text{out}}(\rho) F_{\text{out}}(\rho^{-1}(\mathbf{x} - \mathbf{t})), \quad (\text{B3})$$

where the representation of π depends on F_{in} and F_{out} . If the kernel κ satisfies the following linear constraint, the convolution in (B1) is equivariant.^{59,60,63}

$$\pi_{\text{out}}(\rho) \kappa(\mathbf{x}) = \kappa(\rho \mathbf{x}) \pi_{\text{in}}(\rho). \quad (\text{B4})$$

Following Weiler and Cesa,⁶⁰ the equivariance of the convolution is confirmed:

$$\begin{aligned} \kappa * g_{\text{in}}(F_{\text{in}}) &= \int \kappa(\mathbf{y} - \mathbf{x}) \pi_{\text{in}}(\rho) F_{\text{in}}(\underbrace{\rho^{-1}(\mathbf{x} - \mathbf{t})}_{\mathbf{x}'}) d\mathbf{x}, \\ &= \int \kappa(\mathbf{y} - \mathbf{t} - \rho \mathbf{x}') \pi_{\text{in}}(\rho) F_{\text{in}}(\mathbf{x}') d\mathbf{x}', \\ &= \int \underbrace{\kappa(\rho(\rho^{-1}(\mathbf{y} - \mathbf{t}) - \mathbf{x}'))}_{\pi_{\text{out}}(\rho) \kappa(\rho^{-1}(\mathbf{y} - \mathbf{t}) - \mathbf{x}')} \pi_{\text{in}}(\rho) F_{\text{in}}(\mathbf{x}') d\mathbf{x}', \\ &= \pi_{\text{out}}(\rho) F_{\text{out}}(\rho^{-1}(\mathbf{y} - \mathbf{t})), \\ &= g_{\text{out}}(F_{\text{out}}), \end{aligned} \quad (\text{B5})$$

where the fact that the Jacobian is unity under any transformation of $SE(2)$ is exploited. The constraint (B4) is not only sufficient but also necessary for the equivariance of convolution.⁶³ Moreover, a linear map is equivariant if and only if the map is an equivariant convolution.⁶³ In the derivation of the constraint (B4), the two-dimensionality is not exploited; hence, the same constraint can be derived in the three-dimensional Euclidean space.⁶³

2. Example1: trivial representation with spatially varying kernel

The linear constraint (B4) is interpreted using two simple examples. First, the effect of changes in position is discussed. Consider that the input and output are scalars. Scalar has the trivial representation^{61,62} and $\pi(\rho)$ becomes unity. Consequently, the constraint (B4) becomes

$$\kappa(\mathbf{x}) = \kappa(\rho \mathbf{x}), \quad (\text{B6})$$

where $\kappa(\mathbf{x})$ is a real number depending on \mathbf{x} and $\kappa(\mathbf{x})$ acts on a scalar field.

The rotation in multiples of 120° is considered as an example. A pattern having the wavenumber-3 structure such as $\cos(3\theta)$ is a solution to (B6). Because such a kernel is invariant to the rotation, the output is rotated according to the rotation applied to the input. The radial structure is not determined by (B6); usually, a certain form such as Gaussian is assumed and its amplitude is optimized by training.^{53,60}

There is a trade-off between expressive power and equivariance. For the conventional convolution, a kernel can learn an azimuthal pattern from data, whereas it is not necessarily equivariant. This is in contrast to the equivariant kernels satisfying the constraint (B6).

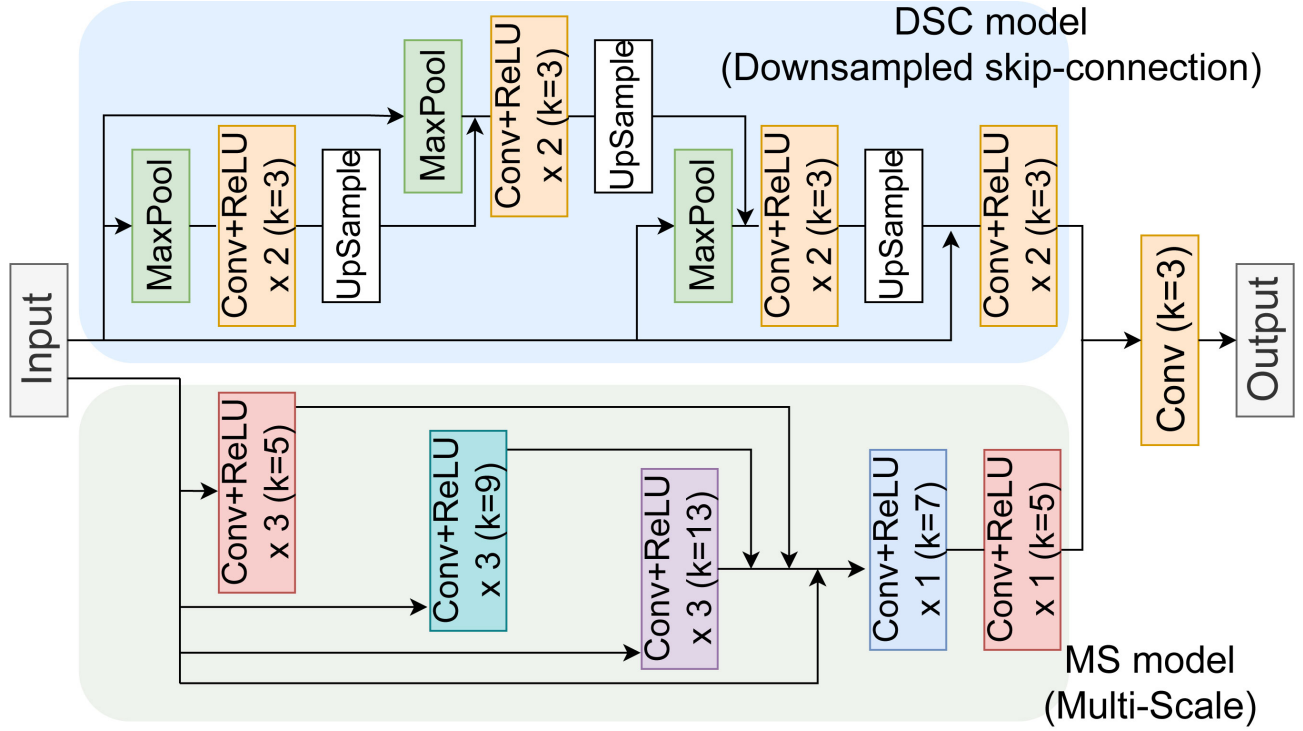


FIG. 15. Network architecture of the hybrid DSC/MS model (Downsampled Skip-Connection and Multi-Scale). The architecture follows the CNN proposed by Fukami et al.²⁵ All convolutions are two-dimensional. The symbol k denotes the spatial size of kernel; for instance, $k = 3$ means that the kernel size is 3×3 . The linear interpolation is used in upsampling.

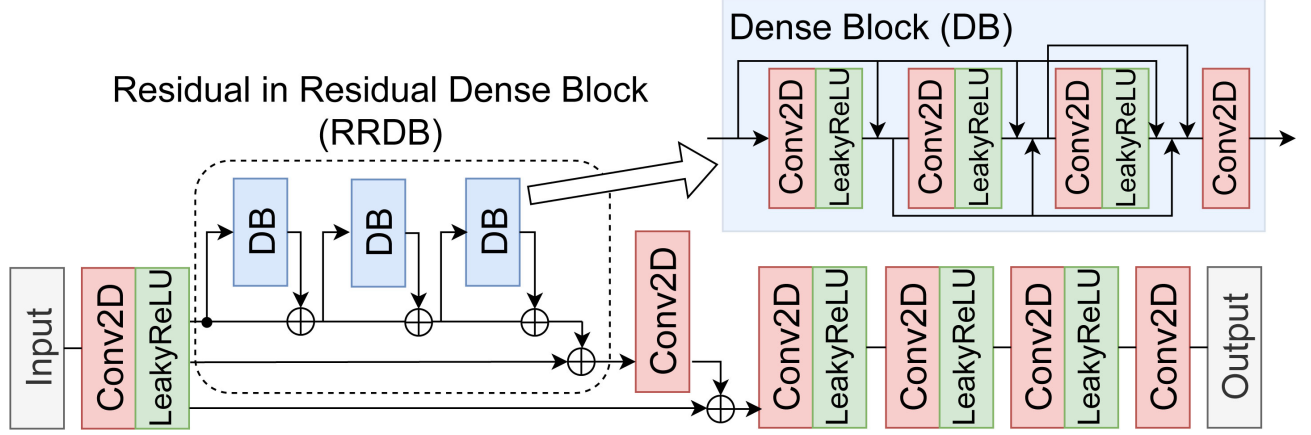


FIG. 16. Network architecture of the RRDN (Residual in Residual Dense Network). The architecture follows the generator of the GAN proposed by Bode et al.³² All kernels in the convolution layers have the spatial size of 3×3 .

3. Example2: C_3 -regular representation with spatially constant kernel

The effect of $\pi(\rho)$ in (B4) is next discussed. Consider that the kernel is spatially constant and the input and output are described using the same regular representation. Equation (B4) is simplified as follows:

$$\pi(\rho)\kappa = \kappa\pi(\rho), \quad (B7)$$

where the subscripts of “out” and “in” are omitted and the matrix κ does not depend on position.

The rotation in multiples of 120° is considered as an example. In the regular representation, the rotation is formulated as a permutation.^{61,62} Figure 17 is a schematic describing the action of the 120° rotation on a set of features. Each component of the features can be considered as a vertex of an equilateral triangle. The rotation is interpreted as the permutation of these vertices.

Mathematically, this set of features $(a, b, c)^T$ is not a geo-

metric vector, even though it is represented by a column vector. In fact, a , b , and c can be complex numbers. The difference between the real and complex representations is discussed in Ref. 60.

The regular representation of C_3 comprises the following three matrices:

$$\pi(\theta = 0) = \begin{pmatrix} 1 & 0 & 0 \\ 0 & 1 & 0 \\ 0 & 0 & 1 \end{pmatrix}, \quad (B8a)$$

$$\pi(\theta = 120^\circ) = \begin{pmatrix} 0 & 0 & 1 \\ 1 & 0 & 0 \\ 0 & 1 & 0 \end{pmatrix}, \quad (B8b)$$

$$\pi(\theta = 240^\circ) = \begin{pmatrix} 0 & 1 & 0 \\ 0 & 0 & 1 \\ 1 & 0 & 0 \end{pmatrix}, \quad (B8c)$$

where the argument of π is denoted by the rotation angle θ instead of the rotation matrix ρ .

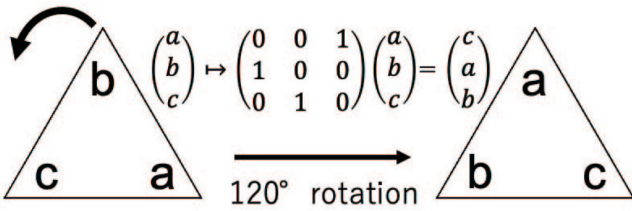


FIG. 17. Schematic describing the action of the 120° rotation on a set of features $(a, b, c)^\top$ with the regular representation. The values of a , b , or c are complex. The matrix $\pi(\theta = 120^\circ)$ in (B8b) acts on these features.

The constraint (B7) must hold for all three matrices of π in (B8). The solution is

$$\begin{pmatrix} \kappa_1 & \kappa_2 & \kappa_3 \\ \kappa_3 & \kappa_1 & \kappa_2 \\ \kappa_2 & \kappa_3 & \kappa_1 \end{pmatrix}, \quad (B9)$$

where κ_1 , κ_2 , and κ_3 are learnable parameters that are determined through training. The kernel (B9) has the symmetric structure, which leads to the commutative property of the kernel multiplication with the permutation representing the rotation (i.e., C_3 -equivariant). The equivariant kernel (B9) has only 3 learnable parameters, though it is a 3×3 matrix. In the conventional convolution, when a kernel is 3×3 , that is, 3 channels are transformed into 3 channels, all 9 parameters are learnable. This is another example of trade-off between expressive power and equivariance.

Appendix C: Details on the spectral nudging method

This section presents the details on the spectral nudging technique^{72,73} used in this study. To introduce a nudging term, the governing equations (5) are represented in the wavenumber space (Section C 1). The covariance to rotation and translation are discussed in Sections C 2 and C 3, respectively. Sec-

tion C 4 describes the configuration of the barotropic instability experiment with the spectral nudging. For simplicity, the infinite Euclidean plane is assumed in Sections C 1-C 3, which results in wavenumbers being continuous.

1. Governing equations in wavenumber space

The governing equations (5) are examined in the Euclidean space before deriving the equations in the wavenumber space. Equations (5a) - (5c) are transformed into the following:

$$\frac{\partial \omega}{\partial t} + \frac{\partial \psi}{\partial x} \frac{\partial \omega}{\partial y} - \frac{\partial \omega}{\partial x} \frac{\partial \psi}{\partial y} = 0, \quad (C1a)$$

$$\nabla^2 \psi = \omega, \quad (C1b)$$

where the viscosity term is omitted for simplicity and ∇ is the gradient operator $\nabla = (\partial_x, \partial_y)^\top$. Using the vertical unit vector e_z , (C1a) can be shown in the geometric formula:

$$\frac{\partial \omega}{\partial t} + e_z \cdot (\nabla \psi \times \nabla \omega) = 0, \quad (C2)$$

where the inner and cross products are used. Equation (C2) clarifies the covariance of the governing equations because this formula is independent of the coordinate system.

The governing equations in the wavenumber space are derived. The Fourier transform ω_k is distinguished with the subscript k from $\omega(x)$. Equations (C1a) and (C1b) are combined into the following⁷⁷:

$$\frac{\partial \omega_k}{\partial t} + \int dl dm a(l, m) \omega_l \omega_m \delta(l + m - k) = 0, \quad (C3a)$$

$$a(l, m) = \frac{(\|l\|^2 - \|m\|^2)(l_x m_y - l_y m_x)}{2\|l\|^2 \|m\|^2}, \quad (C3b)$$

Where k , l , and m are wavenumber vectors (e.g., $k = (k_x, k_y)^\top$) and $\delta(x)$ is the Dirac delta function. The advection term, namely the second term in (C3a), describes triad interactions,⁷⁷ where the coefficient $a(l, m)$ is symmetric with respect to l and m .

To add a nudging term, first, Eqs. (C3) are solved for a lower truncation wavenumber k^L . The obtained solution is denoted by ω_k^L where $\|k\| \leq k^L$. In high-resolution simulations, a nudging term is added to the right-hand side of (C3a):

$$\frac{\partial \omega_k}{\partial t} + \int dl dm a(l, m) \omega_l \omega_m \delta(l + m - k) = -\lambda (\omega_k - \omega_k^L) \chi_{\|k\| \leq k^L}, \quad (C4)$$

where $\chi_{\|k\| \leq k^L}$ is an indicator function, which is equal to 1 when $\|k\| \leq k^L$ and 0 otherwise. Clearly, the nudging term vanishes for higher wavenumbers. The condition of χ can be more complicated. The coefficient $\lambda (> 0)$ generally depends on time or wavenumber, while λ is constant in this study.

2. Covariance to rotation

The covariance of the governing equations (C3a) and (C4) is confirmed with respect to rotation. A wavenumber vector

is transformed in the same manner as that of a position vector because the inner product is invariant: $\mathbf{k} \cdot \mathbf{x} = \mathbf{k}' \cdot \mathbf{x}'$, where $\mathbf{x}' = \rho_\theta \mathbf{x}$, $\mathbf{k}' = \rho_\theta \mathbf{k}$, and ρ_θ is a rotation matrix. The Fourier transform of the vorticity is changed associated with the rotation ($\rho = \rho_\theta$) as follows:

$$\omega_{\mathbf{k}} \rightarrow \omega_{\rho^{-1}\mathbf{k}}, \quad (C5)$$

which corresponds to (3a) in the Euclidean space.

The covariance of (C3a) without the nudging term is examined. The first term is clearly independent of rotation because it is the derivative of the scalar $\omega_{\mathbf{k}}$ with respect to time. The second term also does not change its form under rotation. The delta function is invariant because the condition $\mathbf{l} + \mathbf{m} - \mathbf{k} = \mathbf{0}$ does not depend on the coordinates. The term $l_x m_y - l_y m_x$ is the vertical component of the cross product $\mathbf{l} \times \mathbf{m}$; hence, its form is preserved by two-dimensional rotation. The differential of $d\mathbf{l} d\mathbf{m}$ is invariant because the Jacobian is unity. The other parts in the second term such as $\|\mathbf{l}\|^2$ are invariant because they are scalars. Therefore, the entire equation of (C3a) is covariant with respect to rotation; that is, the form of (C3a) is independent of rotation.

Next, the covariance of (C4) including the nudging term is examined. As the left-hand side of (C4) is the same as that of (C3a), only the right-hand side is discussed. The indicator function is invariant because its condition $\|\mathbf{k}\| \leq k^L$ is described by scalars. The prescribed solution $\omega_{\mathbf{k}}^L$ is covariant because it is a solution of (C3). Therefore, the entire equation (C4) is covariant to rotation. The governing equation does not change its form even when the spectral nudging term is added.

3. Covariance to translation

The covariance with respect to translation is confirmed. The vorticity field $\omega(\mathbf{x})$ is converted to $\omega(\mathbf{x} - \mathbf{r})$ with a given translation vector \mathbf{r} . The Fourier transform is then converted as follows:

$$\omega_{\mathbf{k}} \rightarrow \omega_{\mathbf{k}} e^{-i\mathbf{k} \cdot \mathbf{r}}. \quad (C6)$$

Here, the wavenumber vector \mathbf{k} itself is unchanged under translation.

The governing equation (C3a) is covariant if the following quantity (i.e., the left-hand side) is zero when a translation acts:

$$\frac{\partial \omega_{\mathbf{k}}}{\partial t} + \int d\mathbf{l} d\mathbf{m} a(\mathbf{l}, \mathbf{m}) \omega_{\mathbf{l}} \omega_{\mathbf{m}} \delta(\mathbf{l} + \mathbf{m} - \mathbf{k}). \quad (C7)$$

Owing to the delta function, the coefficient of exponentials of the second term is equal to that of the first term:

$$e^{-i\mathbf{l} \cdot \mathbf{r}} e^{-i\mathbf{m} \cdot \mathbf{r}} \delta(\mathbf{l} + \mathbf{m} - \mathbf{k}) = e^{-i\mathbf{k} \cdot \mathbf{r}} \delta(\mathbf{l} + \mathbf{m} - \mathbf{k}). \quad (C8)$$

This results in (C7) being zero; hence, the governing equation (C3a) does not change the form under translation.

The covariance still holds when the nudging term, namely the right-hand side of (C4), is added. The nudging term is linear with respect to the vorticity and is converted in the same manner as that of the time derivative.

Moreover, the governing equations (C3a) and (C4) are covariant even when a combination of rotation and translation acts because each transformation does not change the forms of the equations.

4. Configuration of the barotropic instability experiment

This subsection describes the configuration of the barotropic instability experiment in Section V B. The configuration is similar to that of the barotropic instability experiment without the spectral nudging in Section III A. The fluid system possesses the symmetries of rotation in 180° and translation along the x direction. In this case, a similar discussion to those in Sections C 1-C 3 is possible if transformations are confined to the subgroup of $SE(2)$.

The LR simulation was performed by numerically solving (C3) with the spectral method as in Section III A. The truncation wavenumber was 10, which determined the alias-free grids of 32×17 . The initial and boundary conditions were the same as in Section III A.

The HR simulation was performed after the LR simulation by numerically solving (C4), where the relaxation constant λ was fixed to 1. The truncation wavenumber was 42 and determined the alias-free grids of 128×65 , which were the same as in Section III A. When calculating the nudging term in (C4), the indicator function was replaced with $\chi_{|k_x| \leq k^L \text{ or } |k_y| \leq k^L}$, which is invariant only to the rotation in multiples of 180° . Further, the linear interpolation in time was employed for the LR solution $\omega_{\mathbf{k}}^L$. This interpolation makes v_n^H dependent on v_n^L in the graphical model of Fig. 14. The initial and boundary conditions were set to be the same as those in the LR simulation.

On varying the random initial condition, 800 and 80 simulations were generated for the training and test, respectively, as in Section III A. In each simulation, 14 snapshots were sampled between $25 \leq t \leq 51$ at intervals of 2. Thus, the training and test datasets comprise 11,200 and 1,120 snapshots, respectively. Test results similar to those shown in Section V B were obtained when the test data were halved or the training data were doubled, implying that the above results are not sensitive to the data size.

Appendix D: Additional analyses

This section presents additional analyses on the decaying turbulence experiment.

1. Dependency on the number of trainable parameters

The test error dependency on the number of trainable parameters is examined. The number of parameters was controlled here by changing the number of channels in the hidden layers. The number of channels was varied by the same factor in all hidden layers. Figure 18 suggests that the equivariant models (Eq-DSC/MS and Eq-RRDN) are more accurate than

the non-equivariant ones when the number of trainable parameters is in the same order. The crosses in the figure denote the original configurations used in Section IV A, where the total sizes of kernels in the convolution are almost the same for Eq-DSC/MS and DSC/MS and for Eq-RRDN and RRDN.

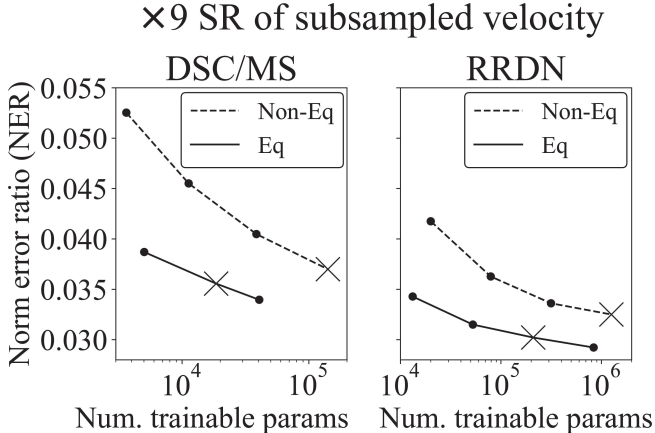


FIG. 18. Norm error ratios (NERs) against various numbers of trainable parameters in the super-resolution model of velocity in the decaying turbulence. The NER is defined by (7). The scale factor s was nine and the low-resolution data were created by subsampling. The crosses stand for the configurations used in Section IV A.

2. Dependency on the size of training data

A smaller number of trainable parameters implies that an equivariant model is trainable with a smaller size of data.¹⁶ Figure 19 shows the NERs against the various sizes of training data. With the decrease in the data size, the NERs tend to increase for all SR models. The NERs of the equivariant models are smaller than those of the non-equivariant ones, and the difference in the NER tends to be larger as the data size is decreased. Therefore, if only a small size of data is available, the equivariant model should be used, that is, the prior knowledge on the geometric symmetry should be incorporated into the neural network design.

3. Dependency on the unit of angle of discrete rotations

In practice, fluid fields need to be discretized for the calculation on computers. The order of discretization of rotations was controlled here by the order N of a cyclic group C_N used in the equivariant CNNs. For instance, if $N = 3$, the unit of angle of rotations is 120° ($= 360^\circ/3$). This subsection demonstrates that the test errors do not necessarily decrease as N is increased, in contrast to that in the image classification.^{52,56,60}

The influence of changing the order of C_N is first examined for the Eq-DSC/MS. The Eq-DSC/MS (and also DSC/MS) has various spatial sizes of kernels in the hidden layers (Fig. 15), which were fixed here. In each layer, the number of sets of the regular representation was fixed. For instance, if both

×9 SR of subsampled velocity

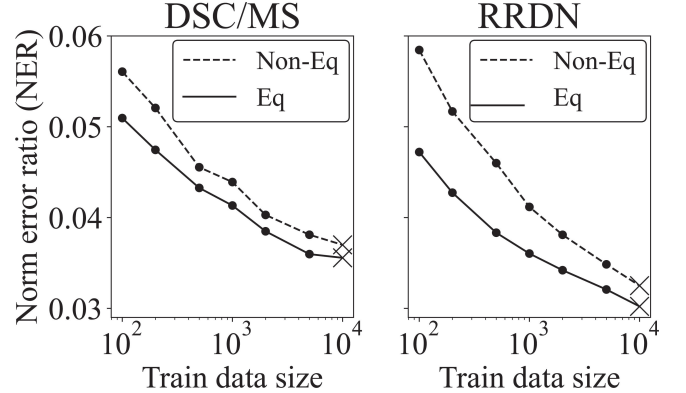


FIG. 19. Norm error ratios (NERs) against various sizes of the training data of the decaying turbulence. The NERs in (7) were calculated from the super-resolved velocity. The train data size means the number of snapshots used in optimizing the SR models. In each configuration, 30% of the total data was used for the validation. The scale factor s was nine and the low-resolution data were created by subsampling. The crosses stand for the configurations used in Section IV A

input and output of a hidden layer are composed of two sets of the regular representation, the number of the input/output channels were 16 for C_8 and 24 for C_{12} . In this preference, as N is increased, the number of trainable parameters increases. Figure 20 shows the NERs and ESEs of C_4 , C_8 , and C_{12} . Although both NER and ESE are the minima in the case of C_8 , the errors are not strongly decreased by increasing the order of C_N .

Eq-DSC/MS: ×9 SR of subsampled velocity

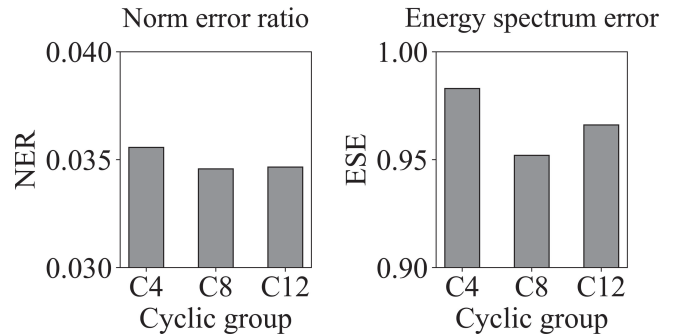


FIG. 20. Norm error ratios (NERs) and energy spectrum errors (ESEs) against the various orders of cyclic group C_N used in the Eq-DSC/MS. The NER and ESE are defined in (7) and (8), respectively. The decaying turbulence velocity was used to create the figure, where the scale factor s was nine and the low-resolution data were created by subsampling.

The spatial size of kernels usually needs to be larger when the order of C_N is increased because the interpolation is used to determine the kernel pattern.^{53,60} The RRDN is appropriate for an experiment varying both C_N and kernel size because all

kernels have the same spatial size (Fig 16). The RRDN consisting of one residual in residual dense block was employed here to reduce the training cost. In each hidden layer, eight sets of the regular representation were used for the input and output. For instance, the number of the input/output channels is 32 for C_4 and 96 for C_{12} . Figure 21 shows the NERs and ESEs against the various C_N and spatial sizes of kernels. The errors are approximately 10% smaller for the 5×5 kernels than those of the 3×3 kernels. This error reduction does not strongly depend on C_N . The errors were also decreased for the non-equivariant RRDN when the 5×5 kernels were used instead of 3×3 . Thus, the decrease in error was comparable between the RRDN and Eq-RRDN. If computational resources are sufficient, the 5×5 kernels should be used for both models. A purpose of this study is to compare the equivariant CNNs with the non-equivariant ones. As a large difference in accuracy was not observed with the 5×5 kernels, the kernels of 3×3 were adopted in Sections IV and V.

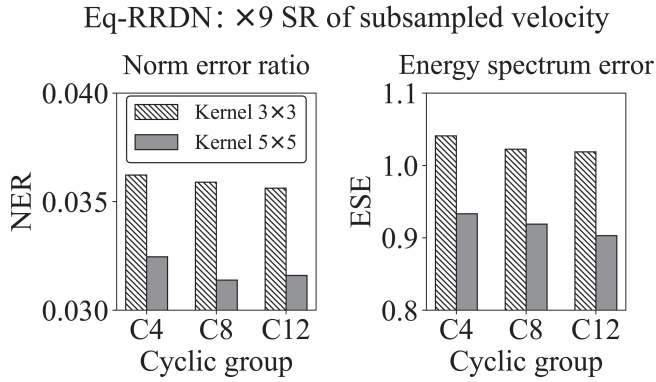


FIG. 21. Norm error ratios (NERs) and energy spectrum errors (ESEs) against the various C_N and spatial sizes of kernels used in the Eq-RRDN. The NER and ESE are defined in (7) and (8), respectively. The decaying turbulence velocity was used to create the figure, where the scale factor s was nine and the low-resolution data were created by subsampling.

4. Comparison of super-resolution between velocity and vorticity

The SR of velocity has been discussed till now. Results similar to those shown above were obtained in the SR of vorticity. This subsection compares the vorticity calculated from the super-resolved velocity with the vorticity that is directly super-resolved. The former is referred to as the velocity-SR, and the latter as vorticity-SR.

Figure 22 compares the test scores between the velocity-SR and vorticity-SR. The vorticity spectrum error (VSE) was calculated instead of the ESE. The VSE is defined as (8), where the energy spectra are replaced with the enstrophy spectra. The scale factor $s = 9$ here; similar figures were obtained for the other s . The NERs are comparable between the velocity-SR and vorticity-SR. In fact, the difference in the NER is limited to approximately 10% (Fig. 22). In contrast, the VSEs of

the velocity-SR are approximately twice as small as those of the vorticity-SR.

Figure 23 compares the energy and enstrophy spectra between the velocity-SR and vorticity-SR. Only the results of the equivariant models (Eq-DSC/MS and Eq-RRDN) are shown because the non-equivariant models (DSC/MS and RRDN) yielded almost the same spectra. The velocity-SR well reproduces the energy and enstrophy spectra over the middle range of wavenumbers $10 \lesssim k \lesssim 25$, compared to those of the vorticity-SR. This result is consistent with the VSE values in Fig. 22. Therefore, it can be concluded that the velocity-SR is more physically valid than the vorticity-SR. Although a direct comparison between the velocity-SR and vorticity-SR is not found in Fukami et al.²⁵, they reported that the L_2 norm error was smaller in the super-resolved velocity than in the super-resolved vorticity. Our result is consistent with theirs.

The lower accuracy of the vorticity-SR may not be attributed to the difference between scalar and vector. The equivariant models incorporate the transformation law of scalars or vectors, which assures that the vorticity calculated from the super-resolved velocity is a scalar field. In contrast, the non-equivariant models do not necessarily provide such a guarantee. Despite this difference, the large spectrum errors are observed in the vorticity-SR regardless of the equivariance and non-equivariance (Figs. 22 and 23). Vorticity fields generally have finer structures owing to the differential operation than velocity fields. The difference in scale might have caused the difference in the accuracy of the super-resolution.

- ¹S. L. Brunton, B. R. Noack, and P. Koumoutsakos, “Machine learning for fluid mechanics,” *Annual Review of Fluid Mechanics* **52**, 477–508 (2020), <https://doi.org/10.1146/annurev-fluid-010719-060214>.
- ²K. Duraisamy, “Perspectives on machine learning-augmented reynolds-averaged and large eddy simulation models of turbulence,” *Phys. Rev. Fluids* **6**, 050504 (2021).
- ³R. Vinuesa and S. L. Brunton, “The potential of machine learning to enhance computational fluid dynamics,” (2021), arXiv:2110.02085 [physics.flu-dyn].
- ⁴S. L. Brunton, “Applying machine learning to study fluid mechanics,” *Acta Mechanica Sinica* (2022), 10.1007/s10409-021-01143-6.
- ⁵M. Raissi, P. Perdikaris, and G. Karniadakis, “Physics-informed neural networks: A deep learning framework for solving forward and inverse problems involving nonlinear partial differential equations,” *Journal of Computational Physics* **378**, 686–707 (2019).
- ⁶K. Kashinath, M. Mustafa, A. Albert, J.-L. Wu, C. Jiang, S. Esmaeilzadeh, K. Azizzadenesheli, R. Wang, A. Chattopadhyay, A. Singh, A. Manepalli, D. Chirila, R. Yu, R. Walters, B. White, H. Xiao, H. A. Tchelepi, P. Marcus, A. Anandkumar, P. Hassanzadeh, and n. Prabhat, “Physics-informed machine learning: case studies for weather and climate modelling,” *Philosophical Transactions of the Royal Society A: Mathematical, Physical and Engineering Sciences* **379**, 20200093 (2021), <https://royalsocietypublishing.org/doi/pdf/10.1098/rsta.2020.0093>.
- ⁷S. Cai, Z. Mao, Z. Wang, M. Yin, George, and E. Karniadakis, “Physics-informed neural networks (PINNs) for fluid mechanics: a review,” *Acta Mechanica Sinica* (2022), 10.1007/s10409-021-01148-1.
- ⁸B. F. Schutz, *Geometrical Methods of Mathematical Physics*, first edition ed. (Cambridge University Press, 1980).
- ⁹M. Nakahara, *Geometry, Topology and Physics*, second edition ed. (CRC Press, 2003).
- ¹⁰P. A. M. Dirac, *General Theory of Relativity* (Princeton University Press, 1996).
- ¹¹M. M. Bronstein, J. Bruna, T. Cohen, and P. Velickovic, “Geometric deep learning: Grids, groups, graphs, geodesics, and gauges,” *CoRR abs/2104.13478* (2021), 2104.13478.

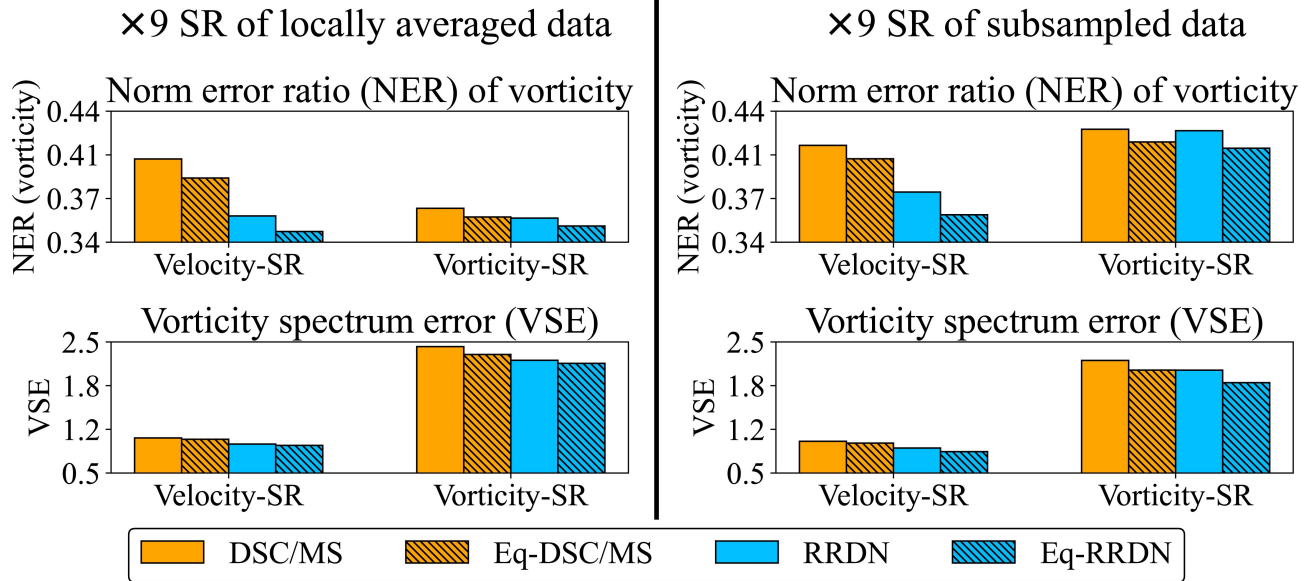


FIG. 22. Norm error ratio (NER) and vorticity spectrum error (VSE) calculated from the super-resolved velocity and vorticity. For “Velocity-SR” the vorticity was calculated from the super-resolved velocity, while for “Vorticity-SR” the vorticity was directly super-resolved. The NER is defined in (7), where the vorticity is evaluated. The VSE is defined as (8), where the energy spectra are replaced with the enstrophy spectra. The scale factor s was nine, that is, the SR models made the resolution nine times finer.

¹²K. Atz, F. Grisoni, and G. Schneider, “Geometric deep learning on molecular representations,” *Nature Machine Intelligence* **3**, 1023–1032 (2021).

¹³L. Gao, Y. Du, H. Li, and G. Lin, “Roteqnet: Rotation-equivariant network for fluid systems with symmetric high-order tensors,” *CoRR abs/2005.04286* (2020), 2005.04286.

¹⁴R. Wang, R. Walters, and R. Yu, “Incorporating symmetry into deep dynamics models for improved generalization.” (2021).

¹⁵J. Suk, P. de Haan, P. Lippe, C. Brune, and J. M. Wolterink, “Equivariant graph neural networks as surrogate for computational fluid dynamics in 3d artery models,” in *Fourth Workshop on Machine Learning and the Physical Sciences (NeurIPS 2021)*. (2021).

¹⁶B. Siddani, S. Balachandar, and R. Fang, “Rotational and reflectional equivariant convolutional neural network for data-limited applications: Multiphase flow demonstration,” *Physics of Fluids* **33**, 103323 (2021), <https://doi.org/10.1063/5.0066049>.

¹⁷J. Han, X.-H. Zhou, and H. Xiao, “Vcnn-e: A vector-cloud neural network with equivariance for emulating reynolds stress transport equations,” (2022), arXiv:2201.01287 [physics.flu-dyn].

¹⁸S. Pawar, O. San, A. Rasheed, and P. Vedula, “Frame invariant neural network closures for kraichnan turbulence,” (2022), arXiv:2201.02928 [physics.flu-dyn].

¹⁹C. Dong, C. C. Loy, K. He, and X. Tang, “Learning a deep convolutional network for image super-resolution,” in *Computer Vision – ECCV 2014*, edited by D. Fleet, T. Pajdla, B. Schiele, and T. Tuytelaars (Springer International Publishing, Cham, 2014) pp. 184–199.

²⁰C. Ledig, L. Theis, F. Huszar, J. Caballero, A. Cunningham, A. Acosta, A. Aitken, A. Tejani, J. Totz, Z. Wang, and W. Shi, “Photo-realistic single image super-resolution using a generative adversarial network,” in *Proceedings of the IEEE Conference on Computer Vision and Pattern Recognition (CVPR)* (2017).

²¹X. Wang, K. Yu, S. Wu, J. Gu, Y. Liu, C. Dong, Y. Qiao, and C. Change Loy, “EsrGAN: Enhanced super-resolution generative adversarial networks,” in *Proceedings of the European Conference on Computer Vision (ECCV) Workshops* (2018).

²²V. K. Ha, J.-C. Ren, X.-Y. Xu, S. Zhao, G. Xie, V. Masero, and A. Hussain, “Deep learning based single image super-resolution: A survey,” *International Journal of Automation and Computing* (2019), 10.1007/s11633-019-1183-x.

²³S. Anwar, S. Khan, and N. Barnes, “A deep journey into super-resolution: A survey,” *ACM Comput. Surv.* **53** (2020), 10.1145/3390462.

²⁴Z. Deng, C. He, Y. Liu, and K. C. Kim, “Super-resolution reconstruction of turbulent velocity fields using a generative adversarial network-based artificial intelligence framework,” *Physics of Fluids* **31** (2019), 10.1063/1.5127031.

²⁵K. Fukami, K. Fukagata, and K. Taira, “Super-resolution reconstruction of turbulent flows with machine learning,” *Journal of Fluid Mechanics* **870**, 106–120 (2019).

²⁶R. Maulik, K. Fukami, N. Ramachandra, K. Fukagata, and K. Taira, “Probabilistic neural networks for fluid flow surrogate modeling and data recovery,” *Phys. Rev. Fluids* **5**, 104401 (2020).

²⁷C. Wang, E. Bentivegna, W. Zhou, L. Klein, and B. Elmegreen, “Physics-informed neural network super resolution for advection-diffusion models,” in *Third Workshop on Machine Learning and the Physical Sciences (NeurIPS 2020)* (2020).

²⁸K. Fukami, K. Fukagata, and K. Taira, “Assessment of supervised machine learning methods for fluid flows,” *Theoretical and Computational Fluid Dynamics* **34**, 497–519 (2020).

²⁹K. Fukami, K. Fukagata, and K. Taira, “Machine-learning-based spatio-temporal super resolution reconstruction of turbulent flows,” *Journal of Fluid Mechanics* **909**, A9 (2021).

³⁰L. Wang, Z. Luo, J. Xu, W. Luo, and J. Yuan, “A novel framework for cost-effectively reconstructing the global flow field by super-resolution,” *Physics of Fluids* **33**, 095105 (2021), <https://doi.org/10.1063/5.0062775>.

³¹B. Liu, J. Tang, H. Huang, and X.-Y. Lu, “Deep learning methods for super-resolution reconstruction of turbulent flows,” *Physics of Fluids* **32**, 025105 (2020).

³²M. Bode, M. Gauding, Z. Lian, D. Denker, M. Davidovic, K. Kleinheinz, J. Jitsev, and H. Pitsch, “Using physics-informed enhanced super-resolution generative adversarial networks for subfilter modeling in turbulent reactive flows,” *Proceedings of the Combustion Institute* **38**, 2617–2625 (2021).

³³H. Kim, J. Kim, S. Won, and C. Lee, “Unsupervised deep learning for super-resolution reconstruction of turbulence,” *Journal of Fluid Mechanics* **910**, A29 (2021).

³⁴C. Jiang, S. Esmaeilzadeh, K. Azizzadenesheli, K. Kashinath, M. Mustafa, H. A. Tchelepi, P. Marcus, M. Prabhat, and A. Anandkumar, “Mesh-freeflownet: A physics-constrained deep continuous space-time super-resolution framework,” in *2020 SC20: International Conference for High Performance Computing, Networking, Storage, and Analysis* (2020), 10.1145/3394501.3394510.

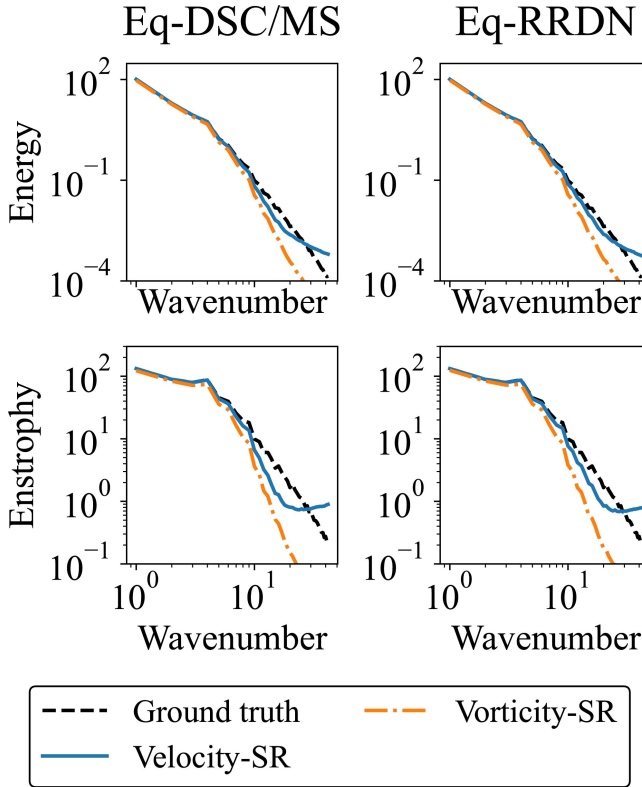


FIG. 23. Ensemble averages of energy and enstrophy spectra at $t = 1.1$ of the decaying turbulence. The time of $t = 1.1$ is the initial time of the test dataset. For “Velocity-SR” the velocity was super-resolved, while for “Vorticity-SR” the vorticity was super-resolved. Only the results of the equivariant models (Eq-DSC/MS and Eq-RRDN) are shown because the non-equivariant models (DSC/MS and RRDN) yielded almost the same spectra. The scale factor s was nine and the subsampled data were used.

Performance Computing, Networking, Storage and Analysis (SC) (IEEE Computer Society, Los Alamitos, CA, USA, 2020) pp. 1–15.

³⁵Y. Xie, E. Franz, M. Chu, and N. Thuerey, “Tempogan: A temporally coherent, volumetric gan for super-resolution fluid flow,” *ACM Trans. Graph.* **37** (2018), 10.1145/3197517.3201304.

³⁶M. Werhahn, Y. Xie, M. Chu, and N. Thuerey, “A multi-pass gan for fluid flow super-resolution,” *Proc. ACM Comput. Graph. Interact. Tech.* **2** (2019), 10.1145/3340251.

³⁷K. Bai, W. Li, M. Desbrun, and X. Liu, “Dynamic upsampling of smoke through dictionary-based learning,” *ACM Trans. Graph.* **40** (2020), 10.1145/3412360.

³⁸E. Ferdinand, A. Suinesiaputra, D. J. Dubowitz, D. Zhao, A. Wang, B. Cowan, and A. A. Young, “4dflownet: Super-resolution 4d flow mri using deep learning and computational fluid dynamics,” *Frontiers in Physics* **8**, 138 (2020).

³⁹L. Sun and J.-X. Wang, “Physics-constrained bayesian neural network for fluid flow reconstruction with sparse and noisy data,” *Theoretical and Applied Mechanics Letters* **10**, 161–169 (2020).

⁴⁰H. Gao, L. Sun, and J.-X. Wang, “Super-resolution and denoising of fluid flow using physics-informed convolutional neural networks without high-resolution labels,” *Physics of Fluids* **33**, 073603 (2021).

⁴¹A. Ducournau and R. Fablet, “Deep learning for ocean remote sensing: an application of convolutional neural networks for super-resolution on satellite-derived sst data,” (2016) pp. 1–6.

⁴²A. J. Cannon, “Quantile regression neural networks: Implementation in r and application to precipitation downscaling,” *Computers and Geosciences* **37**, 1277–1284 (2011).

⁴³T. Vandal, E. Kodra, S. Ganguly, A. Michaelis, R. Nemanic, and A. R. Ganguly, “Deepsd: Generating high resolution climate change projections through single image super-resolution,” (Association for Computing Machinery, 2017) pp. 1663–1672.

⁴⁴E. R. Rodrigues, I. Oliveira, R. Cunha, and M. Netto, “Deepdownscale: A deep learning strategy for high-resolution weather forecast,” (2018) pp. 415–422.

⁴⁵R. Onishi, D. Sugiyama, and K. Matsuda, “Super-resolution simulation for real-time prediction of urban micrometeorology,” *SOLA* **15**, 178–182 (2019).

⁴⁶J. Leinonen, D. Nerini, and A. Berne, “Stochastic super-resolution for downscaling time-evolving atmospheric fields with a generative adversarial network,” *IEEE Transactions on Geoscience and Remote Sensing* , 1–13 (2020).

⁴⁷K. Stengel, A. Glaws, D. Hettinger, and R. N. King, “Adversarial super-resolution of climatological wind and solar data,” *Proceedings of the National Academy of Sciences* **117**, 16805–16815 (2020).

⁴⁸J. Wang, Z. Liu, I. Foster, W. Chang, R. Kettimuthu, and V. R. Kotamarthi, “Fast and accurate learned multiresolution dynamical downscaling for precipitation,” *Geoscientific Model Development* **14**, 6355–6372 (2021).

⁴⁹Y. Yasuda, R. Onishi, Y. Hirokawa, D. Kolomenskiy, and D. Sugiyama, “Super-resolution of near-surface temperature utilizing physical quantities for real-time prediction of urban micrometeorology,” *Building and Environment* **209**, 108597 (2022).

⁵⁰T. Cohen and M. Welling, “Group equivariant convolutional networks,” in *Proceedings of The 33rd International Conference on Machine Learning*, Proceedings of Machine Learning Research, Vol. 48, edited by M. F. Balcan and K. Q. Weinberger (PMLR, New York, New York, USA, 2016) pp. 2990–2999.

⁵¹T. S. Cohen and M. Welling, “Steerable cnns,” 5th International Conference on Learning Representations, ICLR 2017 (2017).

⁵²D. Marcos, M. Volpi, N. Komodakis, and D. Tuia, “Rotation equivariant vector field networks,” in *Proceedings of the IEEE International Conference on Computer Vision (ICCV)* (2017).

⁵³D. E. Worrall, S. J. Garbin, D. Turmukhambetov, and G. J. Brostow, “Harmonic networks: Deep translation and rotation equivariance,” in *Proceedings of the IEEE Conference on Computer Vision and Pattern Recognition (CVPR)* (2017).

⁵⁴Y. Zhou, Q. Ye, Q. Qiu, and J. Jiao, “Oriented response networks,” in *Proceedings of the IEEE Conference on Computer Vision and Pattern Recognition (CVPR)* (2017).

⁵⁵K. T. Schütt, F. Arbabzadah, S. Chmiela, K. R. Müller, and A. Tkatchenko, “Article quantum-chemical insights from deep tensor neural networks,” *Nature Communications* (2017), 10.1038/ncomms13890.

⁵⁶E. J. Bekkers, M. W. Lafarge, M. Veta, K. A. J. Eppenhof, J. P. W. Pluim, and R. Duits, “Roto-translation covariant convolutional networks for medical image analysis,” in *Medical Image Computing and Computer Assisted Intervention – MICCAI 2018*, edited by A. F. Frangi, J. A. Schnabel, C. Davatzikos, C. Alberola-López, and G. Fichtinger (Springer International Publishing, Cham, 2018) pp. 440–448.

⁵⁷I. Sosnovik, A. Moskalev, and A. W. Smeulders, “Scale equivariance improves siamese tracking,” in *Proceedings of the IEEE/CVF Winter Conference on Applications of Computer Vision (WACV)* (2021) pp. 2765–2774.

⁵⁸R. Kondor and S. Trivedi, “On the generalization of equivariance and convolution in neural networks to the action of compact groups,” in *Proceedings of the 35th International Conference on Machine Learning*, Proceedings of Machine Learning Research, Vol. 80, edited by J. Dy and A. Krause (PMLR, 2018) pp. 2747–2755.

⁵⁹T. S. Cohen, M. Geiger, and M. Weiler, “A general theory of equivariant cnns on homogeneous spaces,” in *Advances in Neural Information Processing Systems*, Vol. 32, edited by H. Wallach, H. Larochelle, A. Beygelzimer, F. d’Alché-Buc, E. Fox, and R. Garnett (Curran Associates, Inc., 2019).

⁶⁰M. Weiler and G. Cesa, “General $e(2)$ -equivariant steerable cnns,” in *Advances in Neural Information Processing Systems*, Vol. 32, edited by H. Wallach, H. Larochelle, A. Beygelzimer, F. d’Alché-Buc, E. Fox, and R. Garnett (Curran Associates, Inc., 2019).

⁶¹R. Gilmore, *Lie Groups, Physics, and Geometry: An Introduction for Physicists, Engineers and Chemists* (Cambridge University Press, 2008).

⁶²A. Zee, *Group Theory in a Nutshell for Physicists* (Princeton University Press, 2016).

⁶³M. Weiler, M. Geiger, M. Welling, W. Boomsma, and T. S. Cohen, “3d steerable cnns: Learning rotationally equivariant features in volumetric data,” in *Advances in Neural Information Processing Systems*, Vol. 31, edited by S. Bengio, H. Wallach, H. Larochelle, K. Grauman, N. Cesa-Bianchi, and R. Garnett (Curran Associates, Inc., 2018).

⁶⁴N. Thomas, T. Smidt, S. M. Kearnes, L. Yang, L. Li, K. Kohlhoff, and P. Riley, “Tensor field networks: Rotation- and translation-equivariant neural networks for 3d point clouds,” CoRR **abs/1802.08219** (2018), arXiv:1802.08219.

⁶⁵F. Fuchs, D. Worrall, V. Fischer, and M. Welling, “Se(3)-transformers: 3d roto-translation equivariant attention networks,” in *Advances in Neural Information Processing Systems*, Vol. 33, edited by H. Larochelle, M. Ranzato, R. Hadsell, M. F. Balcan, and H. Lin (Curran Associates, Inc., 2020) pp. 1970–1981.

⁶⁶Y. Xie, Y. Ding, and S. Ji, “Augmented equivariant attention networks for electron microscopy image super-resolution,” CoRR **abs/2011.03633** (2020), 2011.03633.

⁶⁷J. Lee and K. Mu Lee, “Structure-resonant discriminator for image super-resolution,” in *2021 IEEE International Conference on Multimedia and Expo (ICME)* (2021) pp. 1–6.

⁶⁸D. Chen, J. Tachella, and M. E. Davies, “Equivariant imaging: Learning beyond the range space,” in *Proceedings of the IEEE/CVF International Conference on Computer Vision (ICCV)* (2021) pp. 4379–4388.

⁶⁹D. Chen, J. Tachella, and M. E. Davies, “Robust equivariant imaging: a fully unsupervised framework for learning to image from noisy and partial measurements,” CoRR **abs/2111.12855** (2021), 2111.12855.

⁷⁰S. W. Remedios, A. Carass, Y.-T. Wu, J. A. Butman, M. Schär, D. L. Pham, Y. Kim, and J. L. Prince, “Crop-equivariant convolutional neural networks for self-super-resolution,” (2022).

⁷¹J. Ling, A. Kurzawski, and J. Templeton, “Reynolds averaged turbulence modelling using deep neural networks with embedded invariance,” *Journal of Fluid Mechanics* **807**, 155–166 (2016).

⁷²H. von Storch, H. Langenberg, and F. Feser, “A spectral nudging technique for dynamical downscaling purposes,” *Monthly Weather Review* **128**, 3664 – 3673 (2000).

⁷³P. Clark Di Leoni, A. Mazzino, and L. Biferale, “Inferring flow parameters and turbulent configuration with physics-informed data assimilation and spectral nudging,” *Phys. Rev. Fluids* **3**, 104604 (2018).

⁷⁴Y. Yasuda, “equivariant-sr-2d-fluid,” <https://github.com/YukiYasuda2718/equivariant-SR-2D-fluid> (2022).

⁷⁵X. Du, X. Qu, Y. He, and D. Guo, “Single image super-resolution based on multi-scale competitive convolutional neural network,” *Sensors* **18** (2018), 10.3390/s18030789.

⁷⁶Y. Zhang, Y. Tian, Y. Kong, B. Zhong, and Y. Fu, “Residual dense network for image super-resolution,” in *Proceedings of the IEEE Conference on Computer Vision and Pattern Recognition (CVPR)* (2018).

⁷⁷G. K. Vallis, *Atmospheric and Oceanic Fluid Dynamics: Fundamentals and Large-Scale Circulation*, second edition ed. (Cambridge University Press, 2017).

⁷⁸K. Ishioka, “Ispack 1.0.4,” <https://www.gfd-dennou.org/arch/ispack/index.htm.en> (2015).

⁷⁹K. Taira, A. G. Nair, and S. L. Brunton, “Network structure of two-dimensional decaying isotropic turbulence,” *Journal of Fluid Mechanics* **795**, R2 (2016).

⁸⁰M. Yoda, “Super-resolution imaging in fluid mechanics using new illumination approaches,” *Annual Review of Fluid Mechanics* **52**, 369–393 (2020), <https://doi.org/10.1146/annurev-fluid-010719-060059>.

⁸¹M. Matsuo, T. Nakamura, M. Morimoto, K. Fukami, and K. Fukagata, “Supervised convolutional network for three-dimensional fluid data reconstruction from sectional flow fields with adaptive super-resolution assistance,” (2021), arXiv:2103.09020 [physics.flu-dyn].

⁸²R. Keys, “Cubic convolution interpolation for digital image processing,” *IEEE Transactions on Acoustics, Speech, and Signal Processing* **29**, 1153–1160 (1981).

⁸³A. Paszke, S. Gross, F. Massa, A. Lerer, J. Bradbury, G. Chanan, T. Killeen, Z. Lin, N. Gimelshein, L. Antiga, A. Desmaison, A. Kopf, E. Yang, Z. DeVito, M. Raison, A. Tejani, S. Chilamkurthy, B. Steiner, L. Fang, J. Bai, and S. Chintala, “Pytorch: An imperative style, high-performance deep learning library,” in *Advances in Neural Information Processing Systems 32*, edited by H. Wallach, H. Larochelle, A. Beygelzimer, F. d’Alché-Buc, E. Fox, and R. Garnett (Curran Associates, Inc., 2019) pp. 8024–8035.

⁸⁴T. Cohen, M. Weiler, B. Kicanaoglu, and M. Welling, “Gauge equivariant convolutional networks and the icosahedral CNN,” in *Proceedings of the 36th International Conference on Machine Learning*, Proceedings of Machine Learning Research, Vol. 97, edited by K. Chaudhuri and R. Salakhutdinov (PMLR, 2019) pp. 1321–1330.

⁸⁵P. D. Haan, M. Weiler, T. Cohen, and M. Welling, “Gauge equivariant mesh {cnn}s: Anisotropic convolutions on geometric graphs,” in *International Conference on Learning Representations* (2021).

⁸⁶Y. Zhang, K. Li, K. Li, B. Zhong, and Y. Fu, “Residual non-local attention networks for image restoration,” in *International Conference on Learning Representations* (2019).

⁸⁷S. Zhou, J. Zhang, W. Zuo, and C. C. Loy, “Cross-scale internal graph neural network for image super-resolution,” in *Advances in Neural Information Processing Systems* (2020).

⁸⁸J. Gu and C. Dong, “Interpreting super-resolution networks with local attribution maps,” in *Proceedings of the IEEE/CVF Conference on Computer Vision and Pattern Recognition (CVPR)* (2021) pp. 9199–9208.

⁸⁹A. Campa, T. Dauxois, D. Fanelli, and S. Ruffo, *Physics of Long-Range Interacting Systems* (Oxford University Press, 2014).